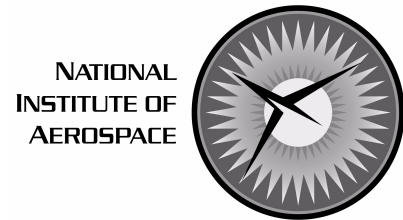
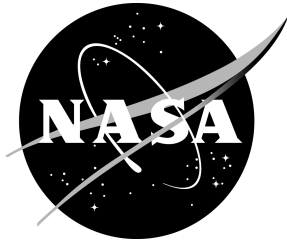


NASA/CR-2004-212684
NIA Report No. 2004-04



Analysis of Composite Skin-Stiffener Debond Specimens Using a Shell/3D Modeling Technique and Submodeling

Ronald Krueger

National Institute of Aerospace, Hampton, Virginia

Pierre J. Minguet

The Boeing Company, Philadelphia, Pennsylvania

July 2004

The NASA STI Program Office . . . in Profile

Since its founding, NASA has been dedicated to the advancement of aeronautics and space science. The NASA Scientific and Technical Information (STI) Program Office plays a key part in helping NASA maintain this important role.

The NASA STI Program Office is operated by Langley Research Center, the lead center for NASA's scientific and technical information. The NASA STI Program Office provides access to the NASA STI Database, the largest collection of aeronautical and space science STI in the world. The Program Office is also NASA's institutional mechanism for disseminating the results of its research and development activities. These results are published by NASA in the NASA STI Report Series, which includes the following report types:

- **TECHNICAL PUBLICATION.** Reports of completed research or a major significant phase of research that present the results of NASA programs and include extensive data or theoretical analysis. Includes compilations of significant scientific and technical data and information deemed to be of continuing reference value. NASA counterpart of peer-reviewed formal professional papers, but having less stringent limitations on manuscript length and extent of graphic presentations.
- **TECHNICAL MEMORANDUM.** Scientific and technical findings that are preliminary or of specialized interest, e.g., quick release reports, working papers, and bibliographies that contain minimal annotation. Does not contain extensive analysis.
- **CONTRACTOR REPORT.** Scientific and technical findings by NASA-sponsored contractors and grantees.

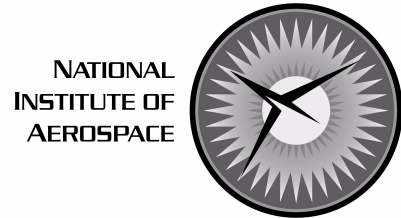
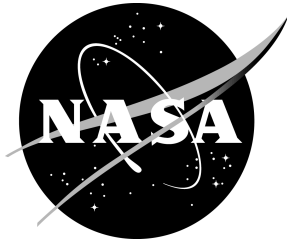
- **CONFERENCE PUBLICATION.** Collected papers from scientific and technical conferences, symposia, seminars, or other meetings sponsored or co-sponsored by NASA.
- **SPECIAL PUBLICATION.** Scientific, technical, or historical information from NASA programs, projects, and missions, often concerned with subjects having substantial public interest.
- **TECHNICAL TRANSLATION.** English-language translations of foreign scientific and technical material pertinent to NASA's mission.

Specialized services that complement the STI Program Office's diverse offerings include creating custom thesauri, building customized databases, organizing and publishing research results . . . even providing videos.

For more information about the NASA STI Program Office, see the following:

- Access the NASA STI Program Home Page at <http://www.sti.nasa.gov>
- Email your question via the Internet to help@sti.nasa.gov
- Fax your question to the NASA STI Help Desk at (301) 621-0134
- Telephone the NASA STI Help Desk at (301) 621-0390
- Write to:
NASA STI Help Desk
NASA Center for Aerospace Information
7121 Standard Drive
Hanover, MD 21076-1320

NASA/CR-2004-212684
NIA Report No. 2004-04



Analysis of Composite Skin-Stiffener Debond Specimens Using a Shell/3D Modeling Technique and Submodeling

Ronald Krueger

National Institute of Aerospace, Hampton, Virginia

Pierre J. Minguet

The Boeing Company, Philadelphia, Pennsylvania

National Aeronautics and
Space Administration

Prepared for Langley Research Center
under Contract NAS1-02117

Langley Research Center
Hampton, Virginia 23681-2199

July 2004

The use of trademarks or names of manufacturers in the report is for accurate reporting and does not constitute an official endorsement, either expressed or implied, of such products or manufacturers by the National Aeronautics and Space Administration.

Available from the following:

NASA Center for AeroSpace Information (CASI)
7121 Standard Drive
Hanover, MD 21076-1320
(301) 621-0390

National Technical Information Service (NTIS)
5285 Port Royal Road
Springfield, VA 22161-2171
(703) 487-4650

ANALYSIS OF COMPOSITE SKIN-STIFFENER DEBOND SPECIMENS USING A SHELL/3D MODELING TECHNIQUE AND SUBMODELING

Ronald Krueger¹ and Pierre J. Minguet²

ABSTRACT

The application of a shell/3D modeling technique for the simulation of skin/stringer debond in a specimen subjected to tension and three-point bending was studied. The global structure was modeled with shell elements. A local three-dimensional model, extending to about three specimen thicknesses on either side of the delamination front was used to model the details of the damaged section. Computed total strain energy release rates and mixed-mode ratios obtained from shell/3D simulations were in good agreement with results obtained from full solid models. The good correlation of the results demonstrated the effectiveness of the shell/3D modeling technique for the investigation of skin/stiffener separation due to delamination in the adherents. In addition, the application of the submodeling technique for the simulation of skin/stringer debond was also studied. Global models made of shell elements and solid elements were studied. Solid elements were used for local submodels, which extended between three and six specimen thicknesses on either side of the delamination front to model the details of the damaged section. Computed total strain energy release rates and mixed-mode ratios obtained from the simulations using the submodeling technique were not in agreement with results obtained from full solid models.

1. BACKGROUND

Many composite components in aerospace structures are made of flat or curved panels with co-cured or adhesively bonded frames and stiffeners. Recent studies focused on the investigation of the debonding mechanism and included testing of skin/stiffener panels and failure analysis using shell models [1-4]. Over the last decade a consistent step-wise approach has been developed which uses experiments to detect the failure mechanism, computational stress analysis to determine the location of first matrix cracking and computational fracture mechanics to investigate the potential for delamination growth. Testing of skin gage stiffened panels designed for pressurized aircraft fuselage has shown that bond failure at the tip of the frame flange is an important and very likely failure mode [5]. Comparatively simple specimens consisting of a stringer flange bonded onto a skin have been developed to study skin/stiffener debonding [6-8]. The failure that initiates at the tip of the flange in these specimens is nearly identical to the failure observed in the full-scale panels and the frame pull-off specimens [7, 9, 10].

During previous analyses of skin/stringer debond specimens two-dimensional finite element models as shown in Figure 1(a) were used because modeling and computational times are shorter compared to full three-dimensional analysis, especially if many different configurations have to be analyzed during the initial design phase of a structure [7, 9, 10].

¹ Senior Staff Scientist, National Institute of Aerospace (NIA), 144 Research Drive, Hampton, VA 23666.

² The Boeing Company, Philadelphia, Pennsylvania

Results from a study where energy release rates from two-dimensional analyses were compared to data from full three-dimensional simulations indicated that plane stress and plane strain models yield upper and lower-bound results [11]. Accurate predictions, however, require the use of three-dimensional models as shown in Figure 1(b). For detailed modeling and analysis of the damage observed during experiments, the shell/3D modeling technique - as shown in Figure 1(c) – is likely to reduce the modeling effort and save computer time because only a relatively small section of interest needs to be modeled with solid elements. The technique combines the accuracy of the full three-dimensional solution with the computational efficiency of a plate or shell finite element model and has been demonstrated for various applications [12-16]. In future applications the shell/3D modeling technique therefore is expected to be used for structural components such as stringer stiffened panels as outlined in Figure 1(d), where the savings in modeling effort and computer time will be even more significant [17].

The first objective of this study is to demonstrate the use of the shell/3D modeling technique for the simulation of skin/stringer debond specimens subjected to tension and three-point bending. A local three-dimensional model, extending to about three specimen thicknesses on either side of the delamination front was used. The transition from shell to solid model was accomplished using a new surface based method in ABAQUS® 6.3 to connect the meshed regions [18]. Delaminations of various lengths were discretely modeled at the locations where delaminations were observed during the experiments. This study complements an investigation of the skin/stringer debond specimen subjected to bending where the connection was based on individual multi point constraints at the shell/solid interface [16, 19].

The second objective of this study is to examine the use of the submodeling technique in ABAQUS® for the simulation of skin/stringer debond specimen subjected to tension and three-point bending. Global models made of shell elements and solid elements were studied. Local submodels were made of solid elements and extended between three and six specimen thicknesses on either side of the delamination front.

For both modeling techniques, mixed mode strain energy release rate distributions were computed across the width of the specimens using the virtual crack closure technique (VCCT) [20, 21]. The results were compared to mixed mode strain energy release rates obtained from computations where the entire specimen had been modeled with solid elements [11, 16, 22].

2. MATERIALS AND TESTING

The current study uses experimental measurements of skin-stiffener debond specimens as reference. The specimens consisted of a bonded skin and flange assembly as illustrated in Figure 2(a) and described in reference [10]. An IM7/8552 graphite/epoxy system was used for both the skin and flange. The skin was made of prepreg tape with a measured average ply thickness of $h = 0.148$ mm and had a [45/-45/0/-45/45/90/90/-45/45/0/45/-45] lay-up. The flange was made of a plain-weave fabric with a thickness of $h = 0.212$ mm. The flange lay-up was [45/0/45/0/45/0/45/0/45]_f, where the subscript “f” denotes fabric, “0” represents a 0°-90° fabric ply and “45” represents a 0°-90° fabric ply rotated by 45° [23]. The measured bondline thickness averaged 0.178mm. Specimens were 25.4-mm wide and 177.8-mm long. The properties of the

graphite/epoxy material and the adhesive were measured at Boeing and are summarized in Table 1.

Four quasi-static tension tests were performed in a servohydraulic load frame in displacement control at a stroke rate of 0.4 mm/min. The specimens were mounted in hydraulic grips with a gage length of 101.6 mm as shown in Figure 2(b). The value of the damage-onset load was averaged from four tests and determined to be $P = 17.8$ kN with a coefficient of variation of 8.9%. Three-point bending tests were performed in a servohydraulic load frame at a monotonic rate of 1.52 mm/min. The bottom support had a span of 101.6 mm as shown in Figure 2(c). The value of the applied load at damage-onset was averaged from four tests and determined to be $Q = 427.6$ N with a coefficient of variation of 12.8%. The tests were terminated when the flange debonded from the skin. Damage was documented from photographs of the polished specimen edges at each of the four flange corners identified in Figure 2(a). Corners 1 and 4 and corners 2 and 3 showed similar damage patterns for both tests. At corners 1 and 4, a delamination running in the bondline (delamination A1) initiated from a matrix crack in the adhesive pocket as shown in Figure 3(a). In two of the quasi-static cases, a second delamination (A2) was observed below the first, in the top $-45^\circ/0^\circ$ skin ply interface. The damage at corners 2 and 3, however, formed first and consisted of a matrix crack in the 45° skin surface ply and a delamination at the $+45^\circ/-45^\circ$ interface as shown in Figure 3(b). Therefore, this damage pattern has been the focus of the current and previous analyses [10, 11, 16, 21, 22].

3. FINITE ELEMENT MODELING

The complex nature of the failure observed during the experiments, where the delamination changed across the specimen width from a delamination running at the skin surface $45^\circ/-45^\circ$ layer interface to a delamination propagating in the bondline (see Figure 3), suggests the need for a three-dimensional model. The current study presents an intermediate step where the local three-dimensional models were created by extruding two-dimensional models across the width. The fact that the delamination changed across the specimen width from a delamination running at the skin surface $45^\circ/-45^\circ$ layer interface to a delamination propagating in the bondline above, however, is still not accounted for in this model. Nevertheless, the three-dimensional model takes width effects into account and therefore provides additional insight into the significance of edge effects.

3.1. Shell/3D Finite Element Model

The first objective of this study is to demonstrate a shell/3D modeling technique for the investigation of delamination onset from an initial crack in the skin/stringer specimen. The shell/3D modeling technique used a local three-dimensional solid finite element model only in the immediate vicinity of the delamination front, as shown in the example of a modeled Double Cantilever Beam (DCB) specimen in Figure 4(a) [15]. The approach combined the accuracy of the full three-dimensional solution with the computational efficiency of a plate or shell finite element model. For a local three-dimensional model, extending to a minimum of about three specimen thicknesses on either side of the delamination front ($d/2h=6.67$), the computed mixed

mode strain energy release rates were within 1% of the results obtained from computations where the entire specimen had been modeled with solid elements as shown in Figure 4(b) [15].

The shell/3D model of the skin/stringer specimen is shown in Figure 5. The outline in Figure 5(a) shows the individual sections and the interface region. The global section was modeled with ABAQUS[®] reduced integrated eight-noded quadrilateral shell elements S8R and the local three-dimensional section was modeled with solid C3D20R elements as shown in Figure 5(b). The local three-dimensional model extended to about three specimen thicknesses on either side of the delamination front as shown in Figure 5(c) since this configuration yielded results which were within 1% of the results obtained from full three-dimensional analysis as described above.

The deformed shell/3D model of the specimen subjected to tension loading with load and boundary conditions is illustrated in Figure 6(a). The deformation is enlarged to visualize the bending of the specimen caused by the load eccentricity in the flange region and the asymmetric layup with respect to the neutral axis. The deformed model of the specimen subjected to three-point bending with load and boundary conditions is shown in Figure 6(b). Both models have identical meshes and differ only in load and boundary conditions. A detail of the modeled delaminated region is shown in Figure 6(c). A refined three-dimensional mesh was used in the critical area of the 45° skin ply where cracking was observed during the tests as shown in Figure 6(c). Outside the refined area, the mesh transitioned rapidly to prevent the three-dimensional model from becoming excessively large. The skin plies were grouped into four layered elements with 45/-45/0, -45/45/90, 90/-45/45 and 0/45/-45 respectively, thus taking advantage of the composite solid element option in ABAQUS[®] [18]. The fabric layers and the resin layer were grouped into five layered elements. In the transition regions several plies were modeled by one element with material properties smeared using the rule of mixtures [24]. This procedure did not calculate the full A-B-D stiffness matrix contributions of the plies [24]; however, it appeared suitable for the small transition regions to enforce a reasonable model size. The transition from the global shell element model to the local three-dimensional model in the vicinity of the delamination front was accomplished by using a new shell to solid coupling option offered by ABAQUS[®] 6.3 to enforce appropriate translations and rotations at the shell-solid interface [18]. Using the shell/3D approach the total number of freedoms could be reduced by more than 12% compared to the full three-dimensional model of the skin/stringer specimen. The efficiency is discussed later.

The shell/3D model shown in Figure 6, however, was not fine enough in the vicinity of the free edges ($z=0.0$ mm and $z=25.4$ mm) to accurately model the effect of the free edges on the distribution of the energy release rates across the width. Therefore, a shell/3D model as shown in Figure 7 was created with twenty elements across the width of the specimen corresponding to the full three-dimensional model discussed in reference [16]. The new shell/3D model was improved by a refined zone (0.74 mm, five elements) near the free edges ($z=0.0$ mm and $z=25.4$ mm) as shown in Figures 7(b) and (c).

The virtual crack closure technique (VCCT) was used to calculate the mode I, II and III components of the strain energy release rate for the modeled delamination [20, 21]. For the entire investigation, the ABAQUS[®] geometric nonlinear analysis procedure was used. This was done in accordance with studies from which reference solutions were taken [11, 16, 22].

3.2 Global Finite Element Model and Submodel

The second objective of this study was to demonstrate the submodeling technique for the investigation of delamination onset from an initial crack in the skin/stringer specimen. The submodeling technique is generally used to study a local part of a model (submodel) with a refined mesh based on interpolation of the solution from an initial, relatively coarse, global mesh. The technique is most useful when it is necessary to obtain an accurate, detailed solution in a local region and the detailed modeling of that local region has negligible effect on the overall solution. One advantage is that different element types can be used in the submodel than those used to model the corresponding region in the global model. This allows the use of shell elements or solid elements for the global model of the specimen and three-dimensional solid elements for the submodel of the delaminated section [18].

An overview of the submodeling technique is given in Figure 8 for the case where shell elements were used to create the global model. The outline in Figure 8(a) shows the physical location of the submodel with respect to the global model of the specimen. To create the global model, the entire skin/stringer specimen was modeled with reduced integrated ABAQUS® four-noded quadrilateral shell elements S4R or reduced integrated eight-noded quadrilateral shell elements S8R as shown in Figure 8(b). The nodes on the submodel boundary where values are defined by interpolating the solution from the global model are called “driven nodes”. The outline in Figure 8(c) shows the location of the driven nodes on both ends of the submodel.

The models used for the case where shell elements were used to create the global model are shown in Figure 9. The deformed global models of the skin/stringer specimen subjected to three-point bending and tension are shown in Figures 9(a) and (b) respectively. The local three-dimensional submodel shown in Figure 9(c) was made of solid C3D20R elements. The local three-dimensional model extended to about three specimen thicknesses on either side of the delamination front and is identical to the local model used in the shell/3D analysis discussed above (see Figure 5(c)). This configuration yielded good results during the initial feasibility study of the shell/3D technique shown in Figure 4. Therefore, the submodel extending about three specimen thicknesses in front and behind the damaged section was used first. In order to determine what portion of the structural component needs to be included in a submodel, another three submodels as shown in Figure 10 were included in this study. The submodels extended about four, five and six specimen thicknesses in front and behind the damaged section.

For the case where solid elements were used to create the global model, an overview of the submodeling technique is given in Figure 11. The outline in Figure 11(a) shows the physical location of the submodel with respect to the global model of the specimen. To create the global model, the entire skin/stringer specimen was modeled with ABAQUS® reduced integrated twenty-noded solid elements C3D20R as shown in Figure 11(b). The outline in Figure 11(c) shows the location of the nodes driven by the solution from the global model on both ends of the submodel. The submodels are identical to those used in the analysis discussed above.

4. FINITE ELEMENT ANALYSIS OF THE SKIN/STRINGER SPECIMEN

4.1. Analysis of the Skin/Stringer Specimen Subjected to Tension Load Using Shell/3D Modeling Technique

4.1.1 Global Response of the Specimen Subjected to Tension Loading

Initially, the global response of the specimens was computed. The load applied to the model is equal to the mean quasi-static damage onset load determined from experiments. The load-displacement and the load-strain behavior computed from different FE models were compared to the corresponding experimental results. This global response was used to examine whether the FE models, the boundary conditions, the loads and the material properties used in the model yielded reasonable results. Strains were averaged from computed nodal point values over a length corresponding to the dimensions of the strain gages shown in Figure 2(a) [10].

The load versus displacement plot in Figure 12 shows that shell/3D model exhibits a stiffer behavior compared to results from the full three-dimensional model. The models also show a slightly stiffer response compared to the experiments (extensometer). This discrepancy may be explained by the fact that the material data used in the FE simulation originated from the literature. For a consistent simulation, material data should be taken from the batch of material that was used to manufacture the specimens. For comparison, results from 2D analysis were included in the plot of Figure 12 [22]. Results from the plane-strain analysis indicated a stiffer behavior. This is caused by the constraints inherent to the plane-strain model, particularly in the $\pm 45^\circ$ plies. The plane-stress model, which imposes the out-of-plane stresses to be zero and allows the strain to be the free parameter, exhibits a more compliant behavior. The influence of the assumptions made in developing two-dimensional finite element models on skin-stiffener debonding specimens was studied in detail in references [22], where geometrically nonlinear finite element analyses using two-dimensional plane-stress and plane-strain elements as well as three different generalized plane strain type approaches were performed.

A comparison of measured strains at the surface of the flange (see Figure 2(a)) and computed results is plotted in Figure 13. In Figure 14, measured strains at the surface of the top 45° skin ply near the flange tip (see Figure 2(a)) and computed surface strains are compared. For both locations, the strains calculated from the shell/3D model are in good agreement with the results from the full three-dimensional finite element model. The models show a slightly stiffer response compared to the strains measured during the experiments. As before, results from 2D analysis were included in the plots of Figure 13 and 14 for comparison [22]. The plane-strain model showed a stiffer behavior yielding an upper bound while the plane-stress models were more compliant, yielding a lower bound.

For the current shell/3D model, the desired reduction in computation time could not be achieved. This is partially caused by the fine three-dimensional mesh in the vicinity of the delaminated region, which was not replaced by shell elements. Additionally, the transition from the global shell element model to the local three-dimensional model was accomplished by multi-point constraints to enforce appropriate translations and rotations at the shell-solid interface, which increased the computation time.

4.1.2. Fractures Mechanics Analysis of the Specimen Subjected to Tension Loading

During a series of nonlinear finite element analyses, strain energy release rates were computed at each front location for the loads applied in the experiments. The computed results were plotted versus the crack length in the center of the specimen ($z=12.7$ mm) as depicted in Figure 15(a) and across the width of the specimen for the longest delamination modeled ($x=31.2$ mm) as depicted in Figure 15(b).

The total energy release rates $G_T=G_I+G_{II}+G_{III}$, along the centerline of the specimen ($z=12.7$ mm) obtained from shell/3D analysis and three-dimensional simulations [16] are plotted in Figure 16 for comparison. After a small initial drop the computed total energy release rate increases sharply with delamination length, reaches a peak value and gradually decreases. The values from the shell/3D analyses are within 3.5% of the results obtained from the full three-dimensional simulations. Improved results may be obtained by enlarging the section modeled with solid elements. The values from plain strain and plane stress analysis are included in Figure 16 for comparison [11, 22]. Qualitatively, all results follow the same trend. As before, the values from plane strain and plane stress analyses form upper and lower bounds except for very short delamination lengths.

The variation of mixed mode ratio G_S/G_T with delamination length is shown in Figure 17. Here G_S denotes the sum of the in-plane shearing components $G_{II}+G_{III}$, and G_T denotes the total energy release rate $G_I+G_{II}+G_{III}$, where G_I is the opening mode. For two-dimensional analyses, where $G_{III}=0$, this definition is equal to the commonly used definition of the mixed mode ratio, G_{II}/G_T . For three-dimensional analysis, which also yields results for the scissoring mode G_{III} , the modified definition of G_S is introduced. The delamination initially starts with high shearing components, followed by a drop, which is equivalent to an increase in G_I . For longer delaminations a gradual increase in shearing components is observed. The values from the shell/3D analysis are in good agreement with the results obtained from the full three-dimensional simulations [16]. The values from plain strain and plane stress analysis were included in Figure 17 for comparison and follow the same trend [11]. The results from three-dimensional analysis in the center of the specimen width ($z=12.7$ mm) show a higher shearing component compared to the results from two-dimensional analysis.

The distribution of the computed total energy release rate G_T across the width (z -coordinate) of the specimen is plotted in Figure 18 for the longest delamination modeled ($x=31.2$ mm). Values at the free edge ($z=0.0$ mm and $z=25.4$ mm) have been excluded from the plot as the model is not fine enough to accurately calculate the energy release rates at the immediate edge. Across the width the computed total energy release rate gradually increases with z before it drops off near the free edge ($z=25.4$ mm). Results from reference [16] - obtained from a full three-dimensional model - have been included in the plot for comparison. The G_T values from the shell/3D analysis are within 6% of the results obtained from the full three-dimensional simulations. The distribution of the mixed-mode ratio G_S/G_T across the width (z -coordinate) of the specimen is plotted in Figure 19 for the same location ($x=31.2$ mm). Across the width the computed mixed mode ratio shows an almost constant value in the center of the specimen with increasing shearing components near the edges ($z=0.0$ mm and $z=25.4$ mm). The plotted mixed-mode ratios are in excellent agreement.

Results obtained from the shell/3D model with a refined mesh near the edges (see Figure 7) are shown in Figures 20 and 21. The distribution of the computed total energy release rate G_T across the width (z -coordinate) of the specimen is plotted in Figure 20 for the longest delamination modeled ($x=31.2$ mm). Across the width the computed total energy release rate gradually increases with z before it first drops off near the free edges and then sharply increases in the zone of the mesh refinement in the immediate vicinity of the free edges ($z=0.0$ mm and $z=25.4$ mm). The model with the refined mesh near the edges yields additional data points where a steep increase in G_T is observed which could not be computed with the model used earlier. Computed energy release rates were omitted where the mesh transitions from coarse to fine, causing two gaps in the distribution at $z \approx 2$ mm and $z \approx 23.5$ mm. The data was omitted from the plot since the post processing algorithm used does not accurately calculate the energy release rate at nodal points which belong to elements with different width. The distribution of the mixed-mode ratio G_S/G_T across the width (z -coordinate) of the specimen is plotted in Figure 21 for the same location ($x=31.2$ mm). Across the width, the computed mixed mode ratio shows high shearing components near the edges, followed by a drop toward the center of the specimen, which is equivalent to an increase in opening mode I. The current model provided a smoother distribution across the width and yielded additional data points near the edges where a steep increase in mixed-mode ratio is observed, which could not be obtained from the coarse model discussed in the previous paragraph. The plotted mixed-mode ratios are in excellent agreement.

A comparison of results obtained from the model with the refined mesh near the edges with results obtained from the model with the coarse mesh is provided Figure 22 for the full 3D analysis, and in Figure 23 for the shell/3D analysis. Results are in excellent agreement and complement each other when considering that the nodal point coordinates along the front are different for both models.

4.2 Analysis of the Skin/Stringer Specimen Subjected to Three-Point Bending Load Using Shell/3D Modeling Technique

The current analysis of the skin/stringer specimen subjected to three-point bending load supplements the study in reference [16]. The focus of the current analysis is the comparison of mixed-mode energy release rates from reference [16] with those obtained using a new shell to solid coupling option offered by ABAQUS® 6.3 [18].

4.2.1. Global Response of the Specimen Subjected to Three-Point Bending Load

The global response of the specimens was computed at the mean quasi-static damage onset load determined from experiments. The load-displacement and the load-strain behavior computed from different FE models were compared to the corresponding experimental results. This global response was used to examine whether the FE models, the boundary conditions, the loads and the material properties used in the models yielded reasonable results. Strains were averaged from computed nodal point values over a length corresponding to the dimensions of the strain gages shown in Figure 2(a) [10].

The load versus displacement data is plotted in Figure 24. Results from the current shell/3D analysis, which used the new surface based option in ABAQUS® to connect the global shell model to the local solid model, are labeled (*SHELL TO SOLID). For comparison, results from reference [16] where the shell and solid regions were connected using multi-point constraints (*MPC) in ABAQUS® were included in the figure. Both shell/3D models are in excellent agreement and exhibit a stiffer behavior compared to results from the full three-dimensional model. The models also predict a slightly stiffer response compared to the experiments (DCDT). This discrepancy may be explained by the fact that the material data used in the FE simulation originated from the literature. For a consistent simulation, material data should be taken from the batch of material that was used to manufacture the specimens. For comparison, results from 2D analysis were included in the plot of Figure 24 [22]. Results from the plane-strain analysis indicated a stiffer behavior. This is caused by the constraints inherent to the plane-strain model, particularly in the $\pm 45^\circ$ plies. The plane-stress model which imposes the out of plane stresses to be zero and allows the strain to be the free parameter exhibits a more compliant behavior compared to results from full three-dimensional analysis.

A comparison of measured strains at the surface of the flange (see Figure 2(a)) and computed results is provided in Figure 25. In Figure 26, measured strains at the surface of the top 45° skin ply near the flange tip (see Figure 2(a)) and computed surface strains were compared. For both locations, the strains calculated from the both shell/3D models are in excellent agreement with the results from the full three-dimensional finite element model. The models show a slightly stiffer response compared to the experiments. As before, results from 2D analysis were included in the plots of Figure 25 and 26 for comparison [22]. The plane-strain model predicted a stiffer behavior, yielding an upper bound, while the plane-stress models were more compliant, yielding a lower bound.

4.2.2. Fractures Mechanics Analysis of the Specimen Subjected to Three-Point Bending Load

The distribution of the computed total energy release rate G_T across the width (z -coordinate) of the specimen is plotted in Figure 27 for the longest delamination modeled ($x=31.2$ mm) as shown in Figure 15(b). Across the width the computed total energy release rate gradually increases with z before it drops off near the free edge ($z = 25.4$ mm). Results from references [22] - obtained from the full three-dimensional models - have been included in the plot for comparison. The G_T values from shell/3D analyses are in excellent agreement and are about 6% lower than the results obtained from the full three-dimensional simulations. The distribution of the mixed-mode ratio G_S / G_T across the width (z -coordinate) of the specimen is plotted in Figure 28 for the same location ($x=31.2$ mm). Across the width the computed mixed mode ratios are in excellent agreement and show an almost constant value with increasing shearing components near the edges ($z=0.0$ mm and $z=25.4$ mm).

For the longest delamination modeled ($x=31.2$ mm), the distribution of the computed total energy release rate G_T across the width (z -coordinate) of the specimen is plotted in Figure 29. Results were obtained from the shell/3D model with a refined mesh near the edges as shown in Figure 7. Across the width, the computed total energy release rate gradually increases

before it first drops off near the free edges and then sharply increases in the zone of the mesh refinement in the immediate vicinity of the free edges ($z=0.0$ mm and $z=25.4$ mm). The model with the refined mesh near the edges yielded additional data points where a steep increase in G_T is observed which could not be computed with the less refined model (Figure 27). The shell/3D yields results are in good agreement with energy release rates obtained from a full 3D model. Computed energy release rates were omitted where the mesh transitions from coarse to fine causing two gaps in the distribution at $z \approx 2$ mm and $z \approx 23.5$ mm. The data was omitted from the plot since the post processing algorithm used does not accurately calculate the energy release rate at nodal points which belong to elements with different width. The distribution of the mixed-mode ratio G_S/G_T across the width (z -coordinate) of the specimen is plotted in Figure 30 for the same location ($x=31.2$ mm). Across the width the computed mixed mode ratio is nearly constant and dominated by opening mode I, but shows high shearing components near the edges, which is caused by the overclosure of the delaminated surface near the edges where the crack opening mode I disappears. The current model provided a smoother distribution across the width and yielded additional data points near the edges where a steep increase in mixed-mode ratio G_S/G_T is observed which could not be computed with the less refined model (Figure 28).

4.3. Analysis of the Skin/Stringer Specimen Subjected to Tension Load Using Submodeling Technique

4.3.1. Computed Displacements and Strains for the Specimen Subjected to Tension Loading

Initially, the global response of the specimens was computed at the mean quasi-static damage onset load determined from experiments. The load-displacement and the load-strain behavior computed from different global models were compared to the corresponding experimental results. This global response was used to examine whether the global models, the boundary conditions, the loads and the material properties used in the model produced reasonable results. Strains were averaged from computed nodal point values over a length corresponding to the dimensions of the strain gages shown in Figure 2(a).

The load versus displacement plot is shown in Figure 31. Results show that both global shell models are in excellent agreement and exhibit a slightly stiffer behavior compared to results from the full three-dimensional global model and results from full 3D analysis published in reference [16]. All FE models show a stiffer response compared to the experiments (extensometer). This discrepancy may be explained by the fact that the material data used in the FE simulation originated from the literature. For a consistent simulation, material data should be taken from the batch of material that was used to manufacture the specimens. Due to matching results, the global model made of S4 elements was not studied further. Further investigations focussed on the global model made of S8R elements.

A comparison of measured strains at the surface of the flange (see Figure 2(a)) and computed results is shown in Figure 32. In Figure 33, measured strains at the surface of the top 45° skin ply near the flange tip (see Figure 2(a)) and computed surface strains were compared. For both locations, the strains calculated from the global shell model are in excellent agreement with the results from the full three-dimensional finite element model. The models show a slightly

stiffer response compared to the strains measured during the experiments. Based on the matching displacements discussed above, the strains from the global solid model were assumed to be identical to the strains obtained from the full 3D analysis of reference [16] and hence were not included in the figures.

The global models made of shell and solid elements appeared to model the displacement and strain behavior of the skin/stringer specimen subjected to tension with sufficient accuracy. Therefore the results from both global models were used as boundary conditions for the local submodels.

4.3.2. Computed Mixed-Mode Strain Energy Release Rates for the Specimen Subjected to Tension Loading

During a series of nonlinear finite element analyses, strain energy release rates were computed at each front location for the loads applied in the experiments. In subsequent analyses results from the global shell model as shown in Figure 9(a) or results from the global solid model as shown in Figure 11(b) were used as boundary conditions for the submodels. For the global shell model, the computed strain energy release rate distributions across the width of the specimen (at $x=31.2$ mm, as shown in Figure 15(b)) are plotted in Figure 34 for different sizes of the submodels as shown in Figures 9 and 10. For the global solid model the computed results are depicted in Figure 35. Values at the free edge ($z=0.0$ mm and $z=25.4$ mm) have been excluded from the plots as the model was not fine enough to accurately model the influence of the free edges on the distribution of the energy release rates. With increasing length of the local three-dimensional submodel, an increase in computed strain energy release rate is observed. However, even for a submodel which extended six specimen thicknesses in front and behind the damaged region, the results did not converge to the values obtained from reference [16] which were included in Figures 34 and 35 for comparison. For the global shell model, the distribution of the mixed-mode ratio G_S/G_T across the width (z -coordinate) of the specimen is plotted in Figure 36 for the same location ($x=31.2$ mm). For the global solid model the computed results are depicted in Figure 37. With increasing length of the local three-dimensional submodel, computed results converge to mixed-mode ratios obtained from reference [16] which were included in Figures 36 and 37 for comparison.

4.4. Analysis of the Skin/Stringer Specimen Subjected to Three-Point Bending Load Using Submodeling

4.4.1. Computed Displacements and Strains for the Specimen Subjected to Three-Point Bending Load

The global response of the specimen was computed at the mean quasi-static damage onset load determined from experiments. The load-displacement and the load-strain behavior computed from different FE models were compared to the corresponding experimental results. This global response was used to examine whether the FE models, the boundary conditions, the loads and the material properties used in the models yielded reasonable results. Strains were

averaged from computed nodal point values over a length corresponding to the dimensions of the strain gages shown in Figure 2(a).

The load versus displacement plot is shown in Figure 38. Results show that both global shell models are in excellent agreement and exhibit a stiffer behavior compared to results from the full three-dimensional global model and the full 3D analysis from reference [16].

A comparison of measured strains at the surface of the flange (see Figure 2(a)) and computed results is shown in Figure 39. In Figure 40, measured strains at the surface of the top 45° skin ply near the flange tip (see Figure 2(a)) and computed surface strains were compared. For both locations, the strains calculated from both global shell models are in excellent agreement with the results from the full three-dimensional finite element model from reference [16]. The models show a slightly stiffer response compared to the strains measured during the experiments. Based on the matching displacements discussed above, the strains from the global solid model were assumed to be identical to the strains obtained from the full 3D analysis from reference [16] and hence were not included in the figures. Due to matching results the global model made of S4 elements was not studied further and the further investigations focused on the global model made of S8R elements.

The global models made of shell and solid elements appeared to model the displacement and strain behavior of the skin/stringer specimen subjected to three-point bending sufficiently accurate. Therefore the results from both global models were used as boundary conditions for the local submodels.

4.3.2. Computed Mixed-Mode Strain Energy Release Rates for the Specimen Subjected to Three-Point Bending Load

During a series of nonlinear finite element analyses, strain energy release rates were computed at each front location for the loads applied in the three-point bending test. In subsequent analyses results from the global shell model as shown in Figure 9(a) or results from a global solid model as shown in Figure 11(b) were used as boundary conditions of the submodels. For the global shell model, the computed strain energy release rate distributions across the width of the specimen (at $x=31.2$ mm, as shown in Figure 15(b)) are plotted in Figure 41 for different sizes of the submodels as shown in Figures 9 and 10. For the global solid model, computed total strain energy release rate distributions across the width (z -coordinate) of the specimen are depicted in Figure 42 at the same location ($x=31.2$ mm) for different sizes of the submodels. Values at the free edge ($z=0.0$ mm and $z=25.4$ mm) have been excluded from the plots, as the model was not fine enough to accurately model the influence of the free edges on the distribution of the energy release rates. With increasing length of the local three-dimensional submodel, an increase of the computed total strain energy release rate is observed. However, even for a submodel which extends six specimen thickness in front and behind the damaged region the results did not converge to the solution obtained from reference [16], which was included in Figures 41 and 42 for comparison. For the local shell model, the distribution of the mixed-mode ratio G_S/G_T across the width (z -coordinate) of the specimen is plotted in Figure 43 for the same location ($x=31.2$ mm). For the global solid model the computed results are depicted in Figure 44. With increasing length of the local three-dimensional submodel, computed results converge to

the solution obtained from reference [16], which was included in Figures 43 and 44 for comparison.

5. SUMMARY AND CONCLUDING REMARKS

The application of the shell/3D modeling technique for the simulation of skin/stringer debond specimen subjected to tension and three-point bending was demonstrated. The study extended the application of this technique beyond the simulation of simple specimens – such as Double Cantilever Beam (DCB), End Notched Flexure (ENF) and Single Leg Bending (SLB) specimens – where the delamination is located between unidirectional plies in the mid-plane of the specimen to a coupon type specimen where the delamination is located between plies of different orientation. The global structure was modeled with shell elements. A three-dimensional model, extending to about three specimen thicknesses on either side of the delamination front was used locally. Delaminations of various lengths were discretely modeled at the locations where delaminations were observed during previous experiments.

Computed strains at the center of the stringer flange were compared with results obtained from full three-dimensional finite element analysis and experimental data. Results from analyses and experiment were in good agreement. Calculated total strain energy release rates and mixed mode ratios obtained from shell/3D simulations also were in good agreement with results obtained from full solid models. Both options offered by ABAQUS® to connect the shell and solid regions yielded almost identical results. The concurrence of the results demonstrated the effectiveness of the shell/3D modeling technique for the investigation of delamination onset from an initial crack. For comparison, results from plane stress and plane strain models provided displacements, flange strains, as well as energy release rates, which formed an upper and lower bound of the results obtained from full three-dimensional or shell/3D simulations.

The current study provided an additional verification step for the shell/3D modeling technique prior to its application to large, full-scale stringer stiffened panels based on the assumption that the failure observed in the skin/stringer specimen is identical to the failure observed in the full-scale panels where the delamination is located between plies of different orientation. For the current shell/3D model, however, the desired reduction in computation time could not be achieved. This is partially caused by the fine three-dimensional mesh in the vicinity of the delaminated region, which was not replaced by shell elements. Additionally, the transition from the global shell element model to the local three-dimensional model was accomplished by multi-point constraints to enforce appropriate translations and rotations at the shell-solid interface, which increased the computation time. As the model size increases, however, gains in efficiency will be more significant. For large, built-up composite structures modeled with plate elements, the shell/3D modeling technique may be used for reducing the model size, compared to a full three-dimensional model, since only a relatively small section in the vicinity of the delamination front needs to be modeled with solid elements. Efficiency gains are expected to be larger for larger models.

The application of the submodeling technique for the simulation of skin/stringer debond in a specimen subjected to tension and three-point bending was also studied. Global models made of shell elements and solid elements were used. Solid elements were used for local

submodels, which extended between three and six specimen thicknesses on either side of the delamination front to model the details of the damaged section. Computed total strain energy release rates did not converge to results obtained from full solid models. Computed mixed-mode ratios however, appeared to slowly converge to the results obtained from full solid models. Based on the current results presented, the submodeling technique cannot be recommended for large, built-up composite structures.

ACKNOWLEDGEMENTS.

The authors gratefully acknowledge Drs. T. Kevin O'Brien and Isabelle Paris for providing insight and experimental results on the specimens analyzed in this paper.

This research was supported and funded by The Boeing Company and the Aviation Applied Technology Directorate as part of the Army's Survivable – Affordable - Repairable – Airframe - Program (SARAP).

REFERENCES

- [1] I.S. Raju, R. Sistla, and T. Krishnamurthy, *Fracture Mechanics Analyses for Skin-Stiffener Debonding*, Eng. Fracture Mech., vol. 54, pp. 371-385, 1996.
- [2] E.H. Glaessgen, I.S. Raju, and C.C. Poe, *Fracture Mechanics Analysis of Stitched Stiffener-Skin Debonding*, in The 39th AIAA/ASME/ASCE/AHS/ASC Structures, Structural Dynamics and Materials Conference, Long Beach, California, AIAA 98-2022, April 20-23, 1998.
- [3] B.G. Falzon, G.A.O. Davies, and E. Greenhalgh, *Failure of thick-skinned stiffener runout sections loaded in uniaxial compression*, Composite Structures, vol. 53, pp. 223-233, 2001.
- [4] J.W.H. Yap, M.L. Scott, R.S. Thomson, and D. Hachenberg, *The analysis of skin-to-stiffener debonding in composite aerospace structures*, Composite Structures, vol. 57, pp. 425-435, 2002.
- [5] P.J. Minguet, M.J. Fedro, T.K. O'Brien, R.H. Martin, and L.B. Ilcewicz, *Development of a Structural Test Simulating Pressure Pillowing Effects in Bonded Skin/Stringer/Frame Configuration*, in Proceedings of the Fourth NASA/DoD Advanced Composite Technology Conference, Salt Lake City, Utah, 1993.
- [6] P.J. Minguet and T.K. O'Brien, *Analysis of Composite Skin/Stringer Bond Failures Using a Strain Energy Release Rate Approach*, in The Tenth International Conference on Composite Materials, vol. I, A. Poursartip and K. Street, Eds., 1995, pp. 245-252.
- [7] P.J. Minguet and T.K. O'Brien, *Analysis of Test Methods for Characterizing Skin/Stringer Debonding Failures in Reinforced Composite Panels*, in Composite Materials: Testing and Design (Twelfth Volume), ASTM STP 1274, R.B. Deo and C.R. Saff, Eds., 1996, pp. 105-124.
- [8] P.J. Minguet, *Analysis of the Strength of the Interface Between Frame and Skin in a Bonded Composite Fuselage Panel*, in The 38th AIAA/ASME/ASCE/AHS/ASC Structures, Structural Dynamics and Materials Conference, 1997, pp. 2783-2790.
- [9] R. Krueger, M.K. Cvitkovich, T.K. O'Brien, and P.J. Minguet, *Testing and Analysis of Composite Skin/Stringer Debonding Under Multi-Axial Loading*, Journal of Composite Materials, vol. 34, pp. 1263-1300, 2000.

- [10] R. Krueger, I.L. Paris, T.K. O'Brien, and P.J. Minguet, *Fatigue Life Methodology for Bonded Composite Skin/Stringer Configurations*, Journal of Composites Technology and Research, vol. 24, pp. 56-79, 2002.
- [11] R. Krueger, I.L. Paris, T.K. O'Brien, and P.J. Minguet, *Comparison of 2D Finite Element Modeling Assumptions with Results from 3D Analysis for Composite Skin-Stiffener Debonding*, Composite Structures, vol. 57, pp. 161-168, 2002.
- [12] C.G. Dávila, *Solid-to-Shell Transition Elements for the Computation of Interlaminar Stresses*, Computing Systems in Engineering, vol. 5, pp. 193-202, 1994.
- [13] J.T. Wang, C.G. Dávila, D.W. Sleight, and T. Krishnamurthy, *Crown Panel Stiffener-Frame Intersection Structural Integrity Analyses*, presented at 5th NASA/DoD Conference on Advanced Composites Technology, Seattle, WA, 1994.
- [14] R. Krueger and T.K. O'Brien, *A Shell/3D Modeling Technique for the Analysis of Delaminated Composite Laminates*, NASA/TM-2000-210287, ARL-TR-2207, June 2000.
- [15] R. Krueger and T.K. O'Brien, *A Shell/3D Modeling Technique for the Analysis of Delaminated Composite Laminates*, Composites Part A: Applied Science and Manufacturing, vol. 32, pp. 25-44, 2001.
- [16] R. Krueger and P.J. Minguet, *Analysis of Composite Skin-stiffener Debond Specimens Using Volume Elements and a Shell/3D Modeling Technique*, NASA/CR-2002-211947, ICASE Report No. 2002-38, October 2002.
- [17] R. Krueger, T.K. O'Brien, and P.J. Minguet, *Implementation of Interlaminar Fracture Mechanics In Design: An Overview*, presented at ICCM-14, San Diego, SME Technical Paper EM03-384, 2003.
- [18] *ABAQUS/Standard - User's Manual - Version 6.3*, vol. II: Hibbitt, Karlsson & Sorensen, Inc., 2002.
- [19] *ABAQUS/Standard - User's Manual - Version 5.6*, vol. II: Hibbitt, Karlsson & Sorensen, Inc., 1996.
- [20] E.F. Rybicki and M.F. Kanninen, *A Finite Element Calculation of Stress Intensity Factors by a Modified Crack Closure Integral*, Eng. Fracture Mech., vol. 9, pp. 931-938, 1977.
- [21] R. Krueger, *Virtual Crack Closure Technique: History, Approach and Applications*, Applied Mechanics Reviews, vol. 57, pp. 109-143, 2004.
- [22] R. Krueger and P.J. Minguet, *Influence of 2D Finite Element Modeling Assumptions on Debonding Prediction For Composite Skin-Stiffener Specimens Subjected to Tension and Bending*, NASA/CR-2002-211452, ICASE Report No. 2002-4, March 2002.
- [23] *ASTM D 3878-02, Standard Terminology for Composite Materials*, in Annual Book of ASTM Standards, vol. 15.03: American Society for Testing and Materials, 2002.
- [24] S.W. Tsai and H.T. Hahn, *Introduction to Composite Materials*: Technomic Publishing Co., Inc., 1980.

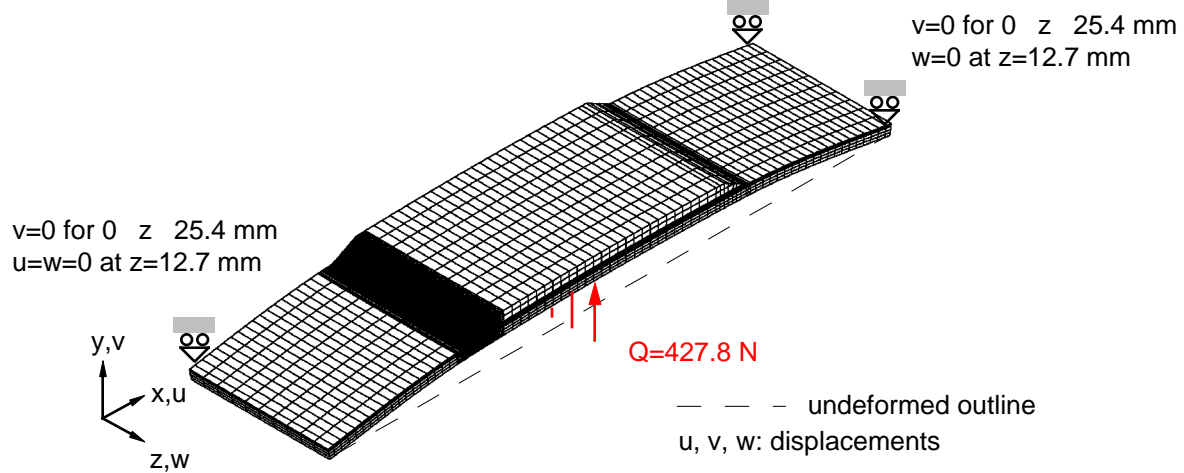
Table 1.
Material Properties

IM7/8552 Unidirectional Graphite/Epoxy Prepreg		
$E_{11} = 161.0 \text{ GPa}$	$E_{22} = 11.38 \text{ GPa}$	$E_{33} = 11.38 \text{ GPa}$
$\nu_{12} = 0.32$	$\nu_{13} = 0.32$	$\nu_{23} = 0.45$
$G_{12} = 5.17 \text{ GPa}$	$G_{13} = 5.17 \text{ GPa}$	$G_{23} = 3.92 \text{ GPa}$
IM7/8552 Graphite/Epoxy Plain Weave Fabric		
$E_{11} = 71.7 \text{ GPa}$	$E_{22} = 71.7 \text{ GPa}$	$E_{33} = 10.3 \text{ GPa}$
$\nu_{12} = 0.04$	$\nu_{13} = 0.35$	$\nu_{23} = 0.35$
$G_{12} = 4.48 \text{ GPa}$	$G_{13} = 4.14 \text{ GPa}$	$G_{23} = 4.14 \text{ GPa}$
Grade 5 FM300 Adhesive		
$E = 1.72 \text{ GPa}$	$\nu = 0.3$	(assumed isotropic)

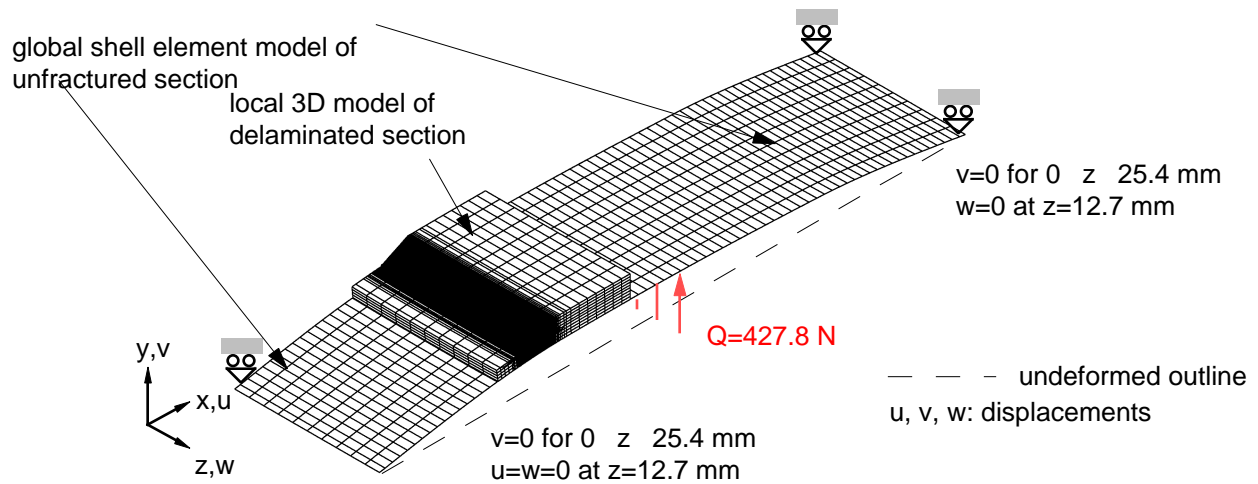
The material properties are given with reference to the ply coordinate axes where index 11 denotes the ply principal axis that coincides with the direction of maximum in-plane Young's modulus (fiber direction). Index 22 denotes the direction transverse to the fiber in the plane of the lamina and index 33 the direction perpendicular to the plane of the lamina.



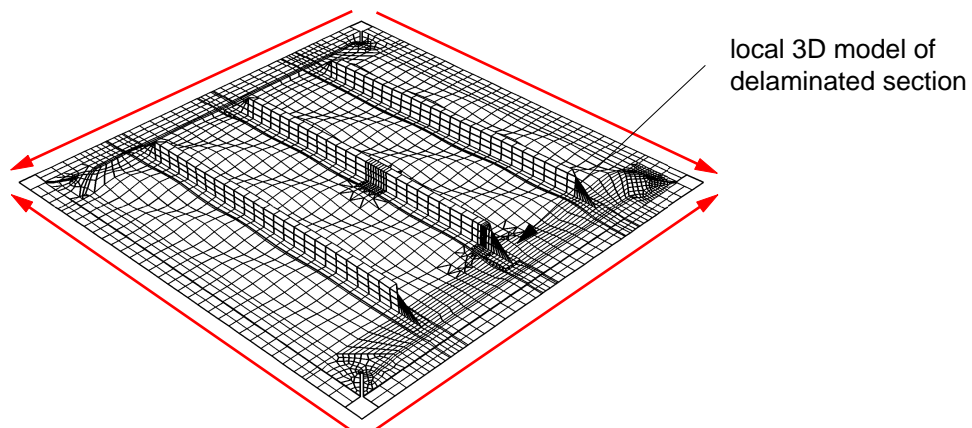
(a) Deformed two-dimensional model of skin/stringer specimen (101.6 mm x 25.4 mm) [10].



(b) Deformed three-dimensional model of skin/stringer specimen (101.6 mm x 25.4 mm) [11].

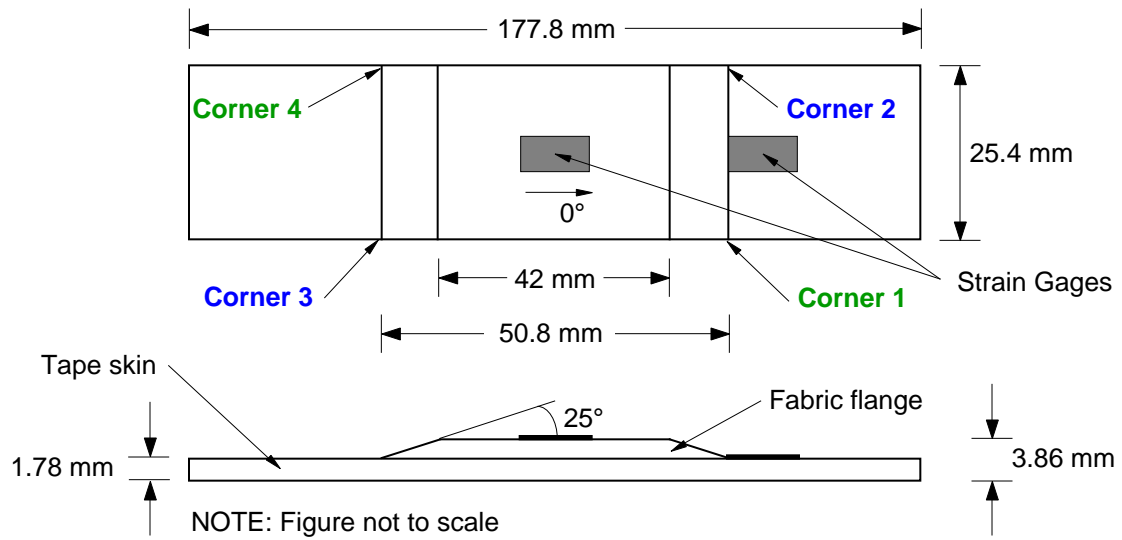


(c) Deformed shell/3D model of skin/stringer specimen (101.6 mm x 25.4 mm) [16].

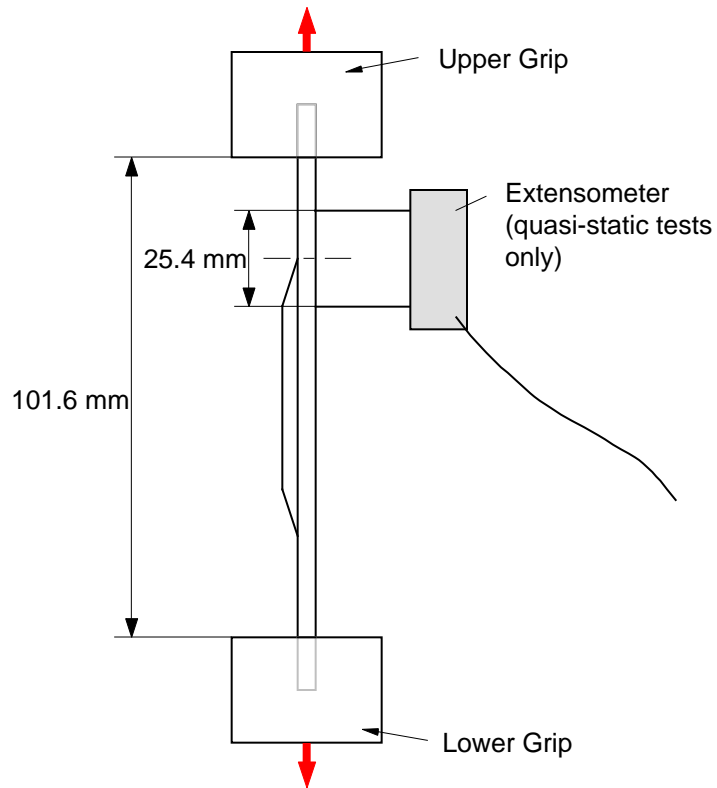


(d) Full Size Stringer Stiffened Panel (1016 mm x 1016 mm)[17].

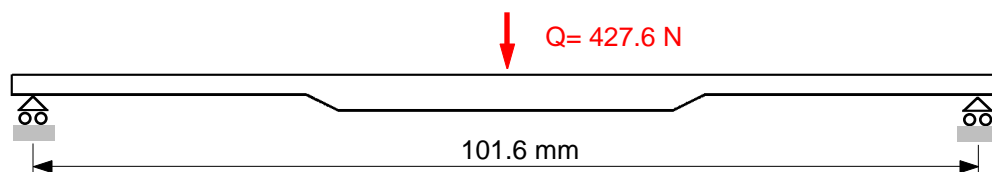
Figure 1. Finite Element Modeling.



(a). Specimen configuration.

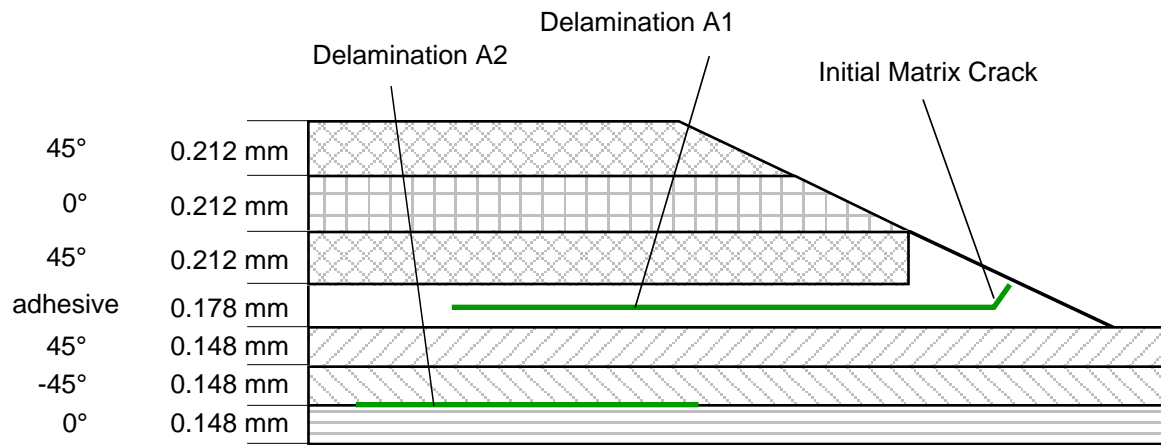


(b). Tension test set-up.



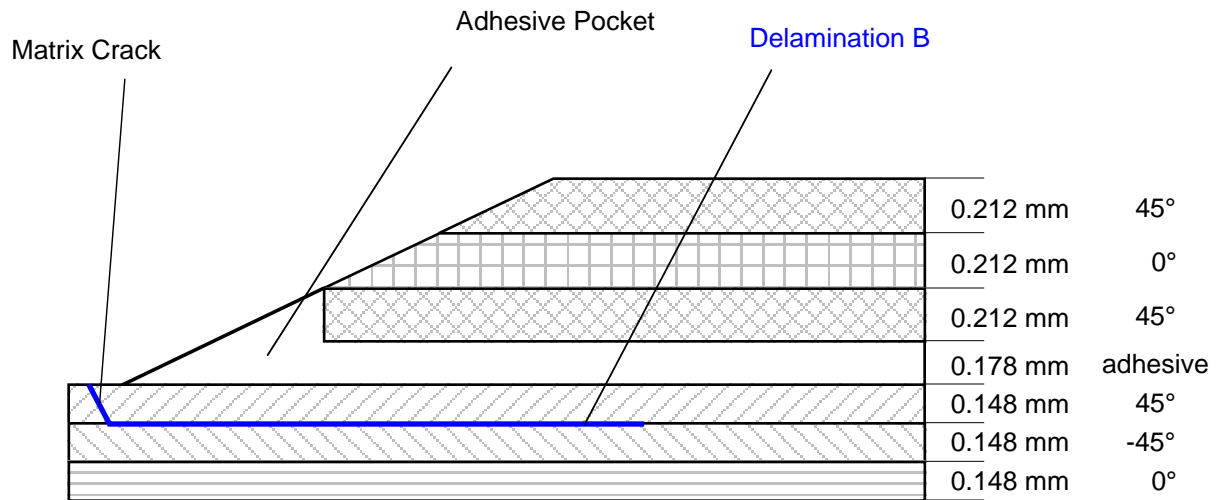
(c). Three-point bending case.

Figure 2. Specimen configuration and test set-up.



dimensions not to scale!

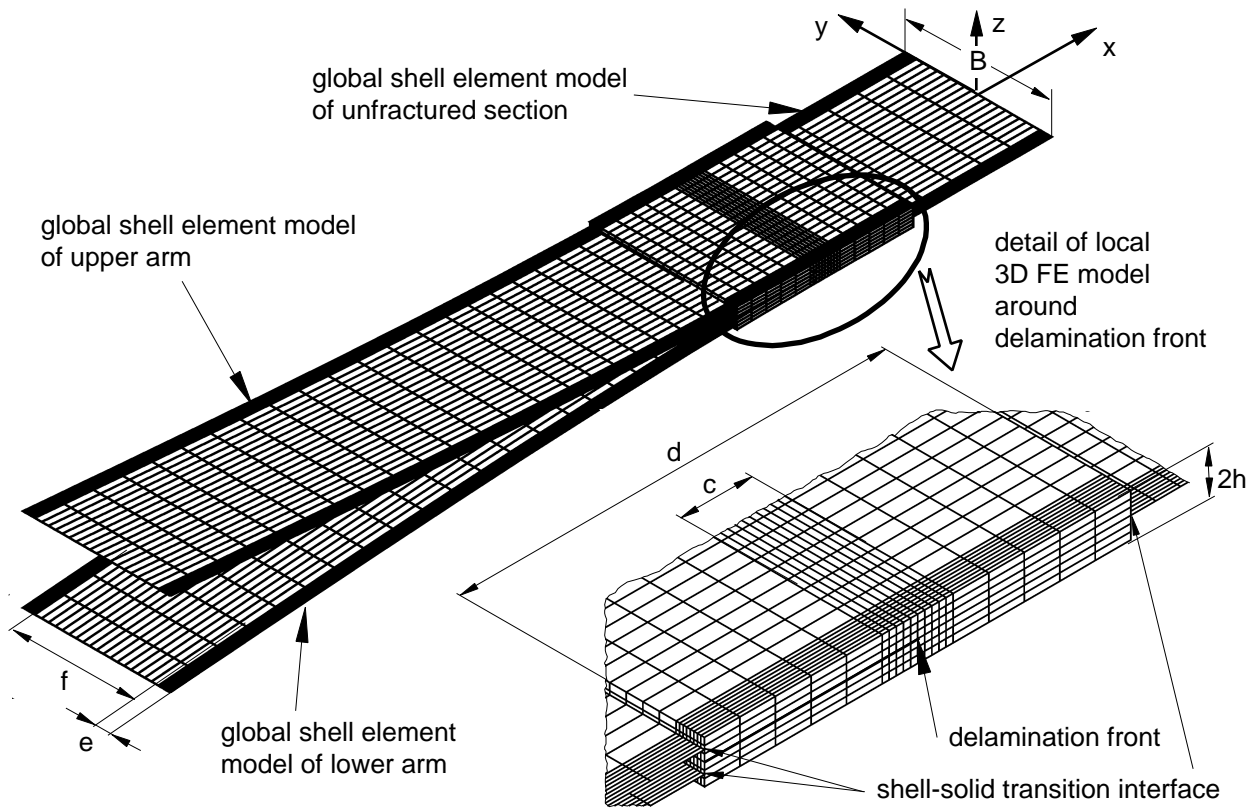
(a). Typical damage patterns observed at specimen corners 1 and 4.



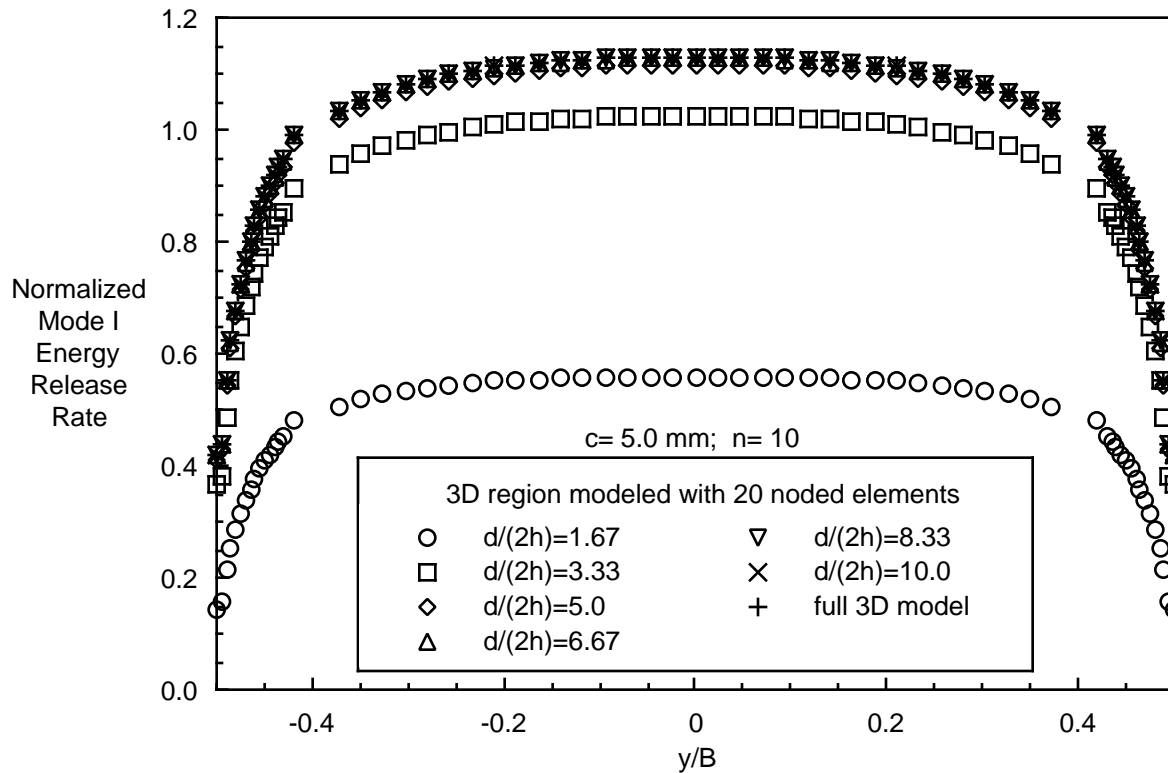
dimensions not to scale!

(b). Typical damage patterns observed at specimen corners 2 and 3.

Figure 3. Typical damage patterns observed in skin/stringer specimen [10].

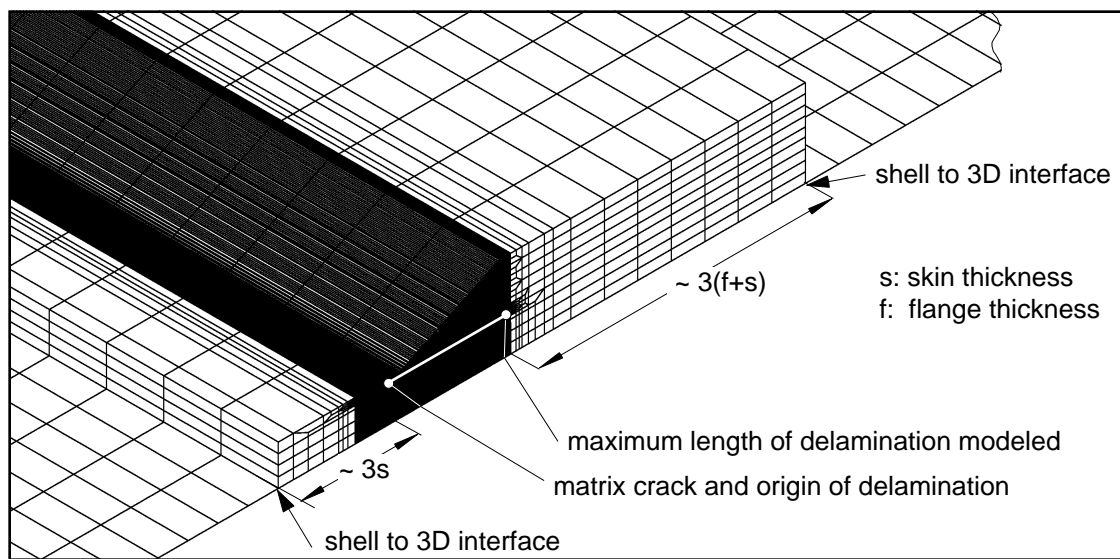
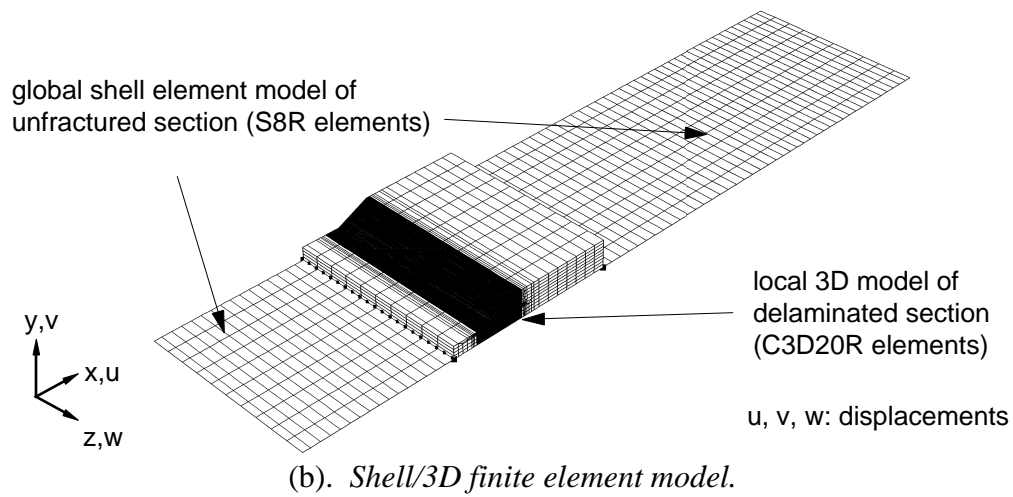
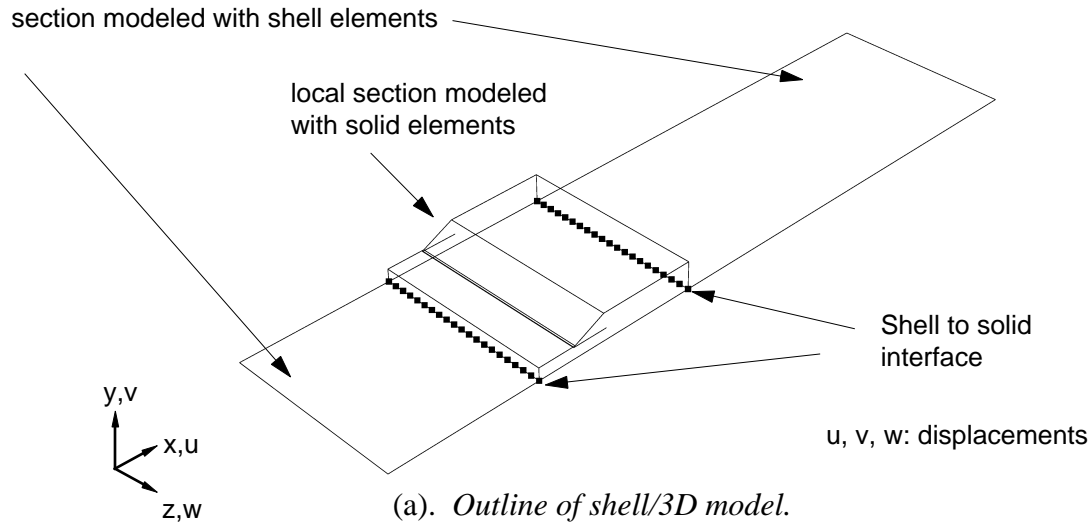


(a). FE model and detail around delamination front
($c = 5 \text{ mm}$, $d = 30 \text{ mm}$, $e = 2 \text{ mm}$, $f = 21.0 \text{ mm}$, $2h = 3.0 \text{ mm}$, $B = 25.0 \text{ mm}$).



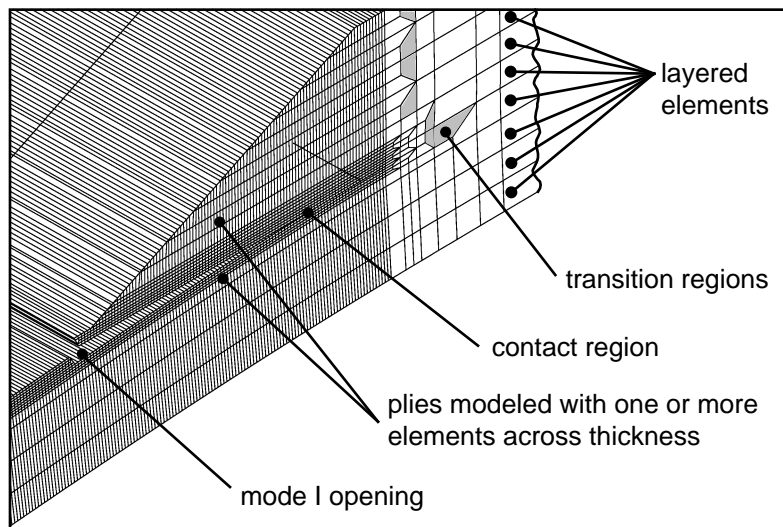
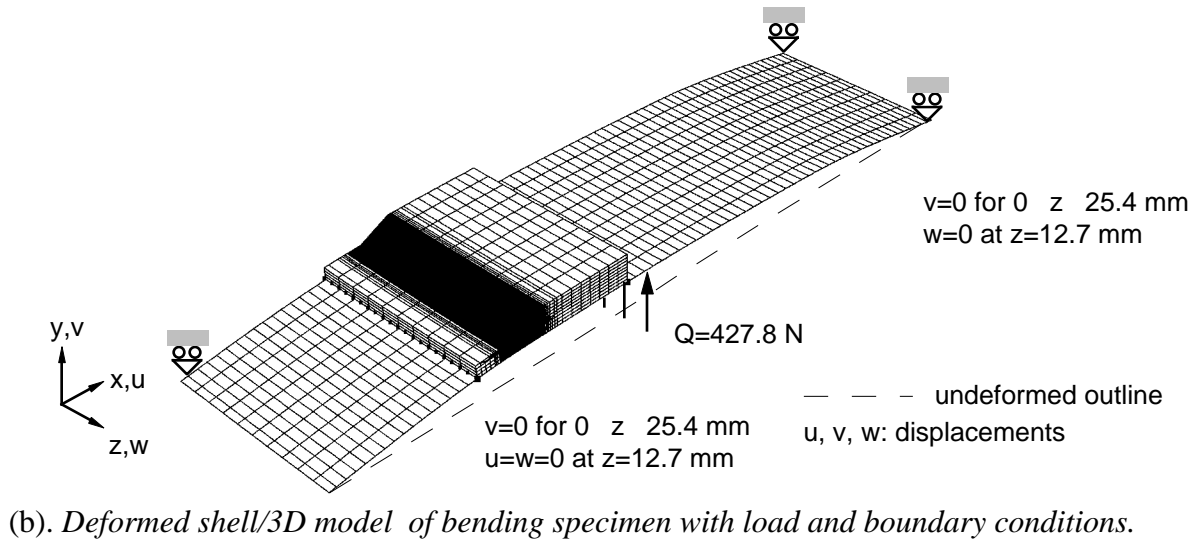
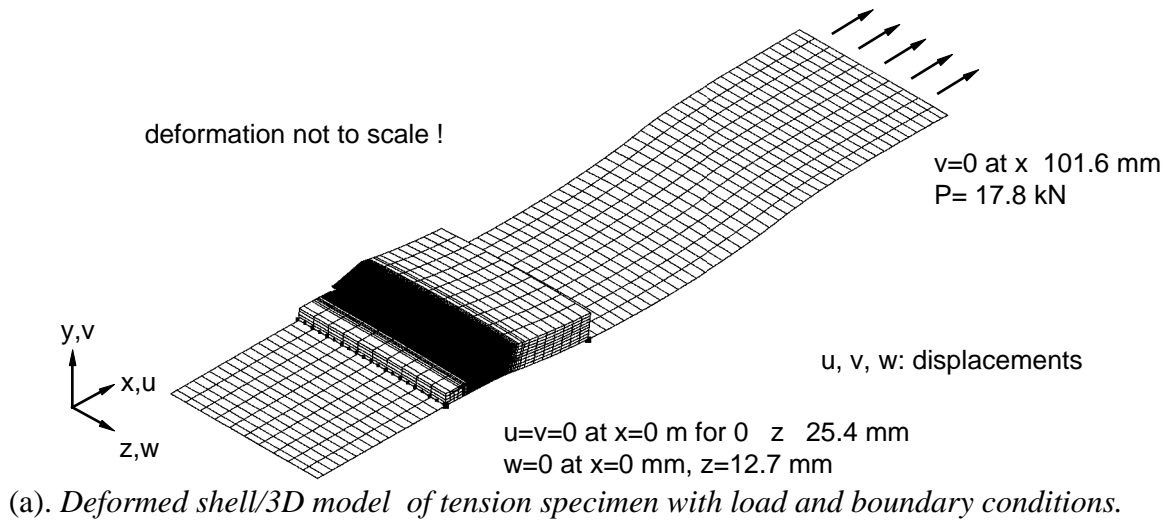
(b). Strain energy release rate distribution across the width.

Figure 4. Shell/3D Finite element model of a DCB Specimen with $[0]_{24}$ layup [15].

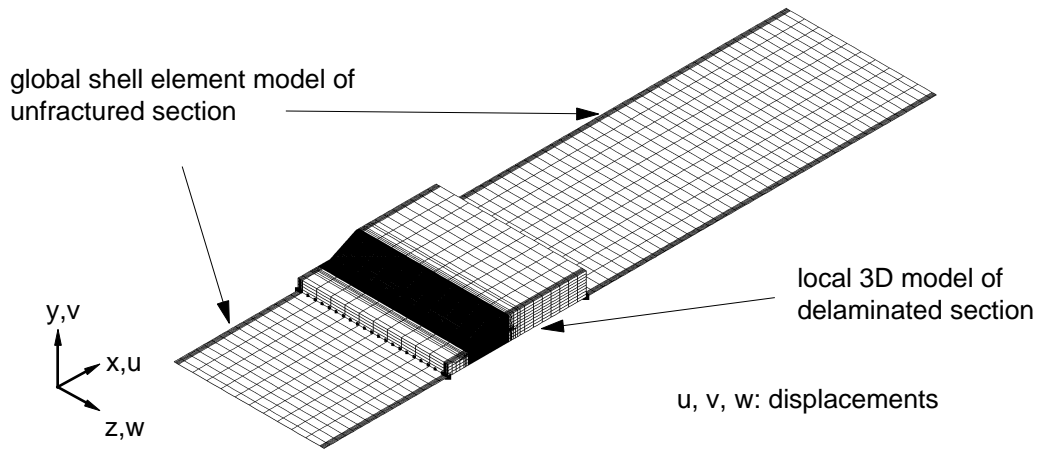


(c). Detail of undeformed local 3D model and shell to 3D interface region.

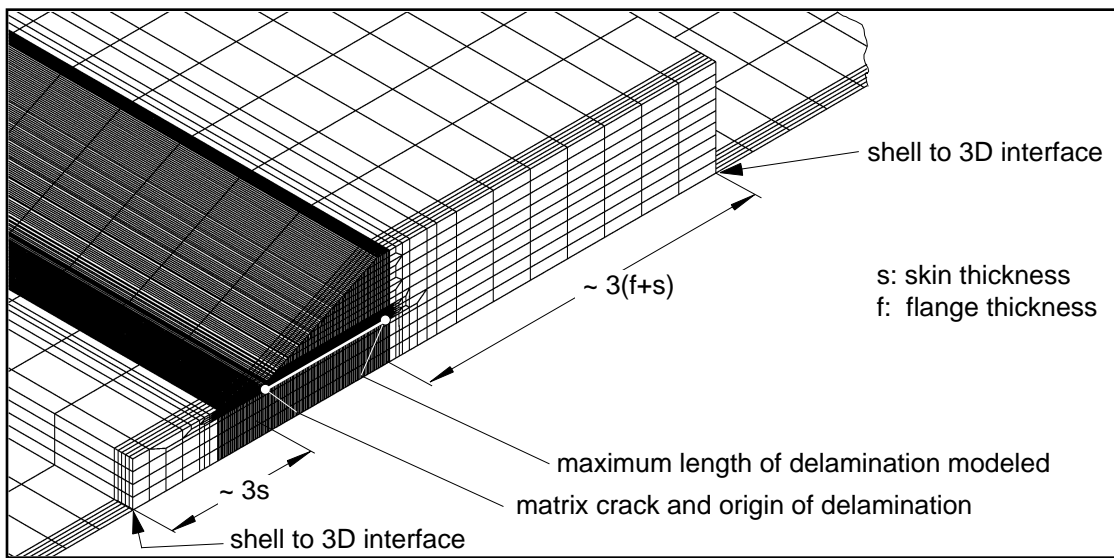
Figure 5. Shell/3D model of skin/flange specimen.



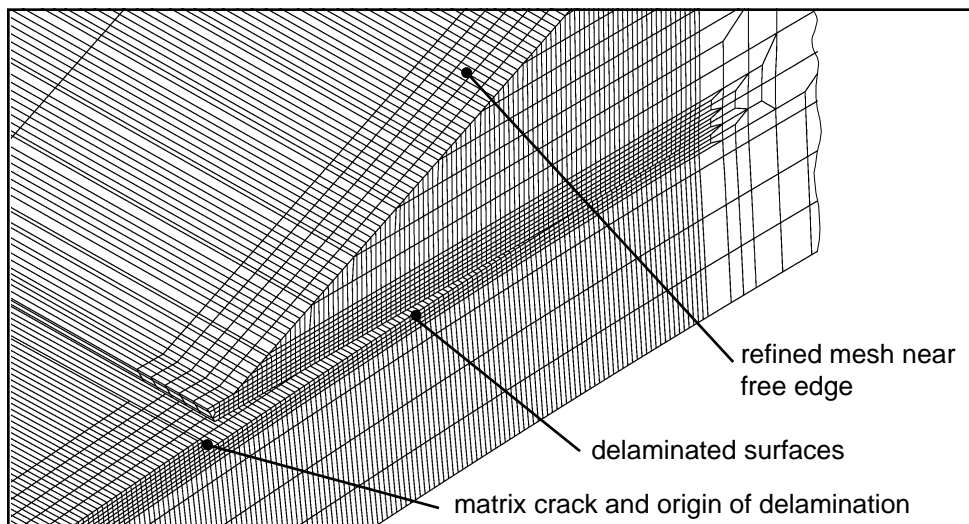
(c). Detail of deformed model of damaged specimen.
 Figure 6. Deformed shell/3D model of skin/flange specimen.



(a). Deformed shell/3D model with load and boundary conditions.

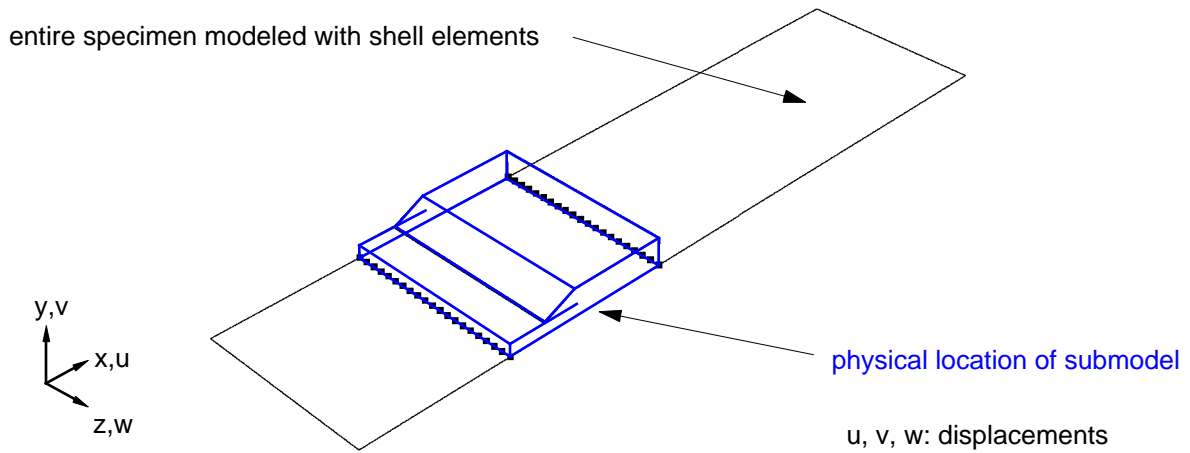


(b). Detail of undeformed local 3D model and shell to 3D interface region.

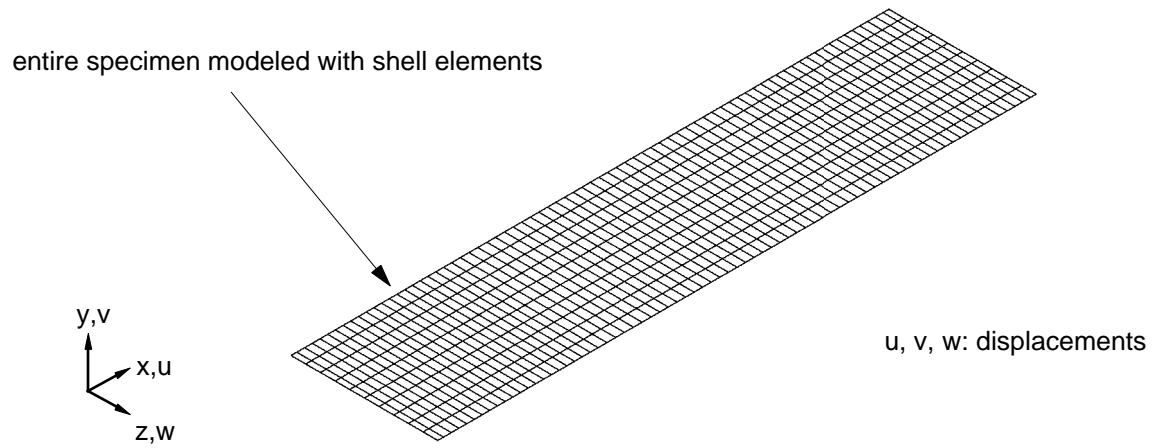


(c). Detail of deformed model of damaged specimen.

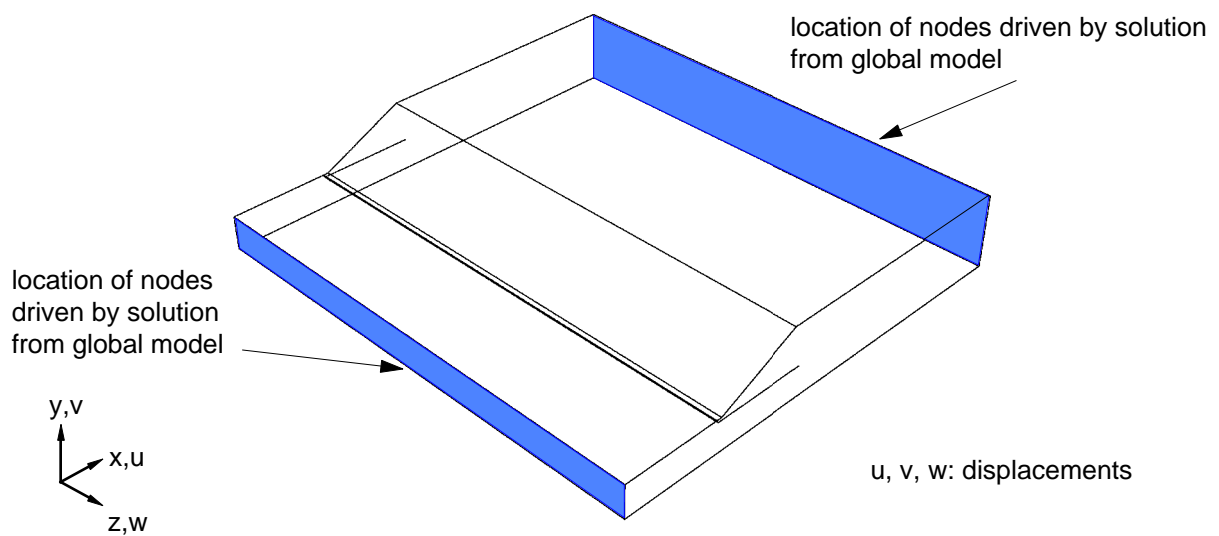
Figure 7. Shell/3D model of skin/flange specimen with fine mesh near the edge.



(a). Outline of submodelling technique using shell elements for global model and solid elements for the submodel.

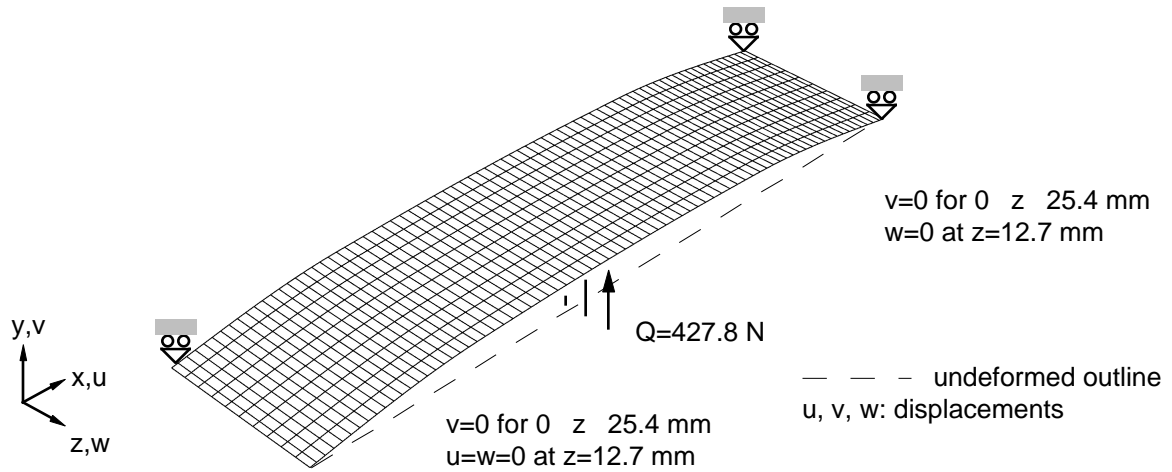


(b). Global model of skin/flange specimen modeled with shell elements.

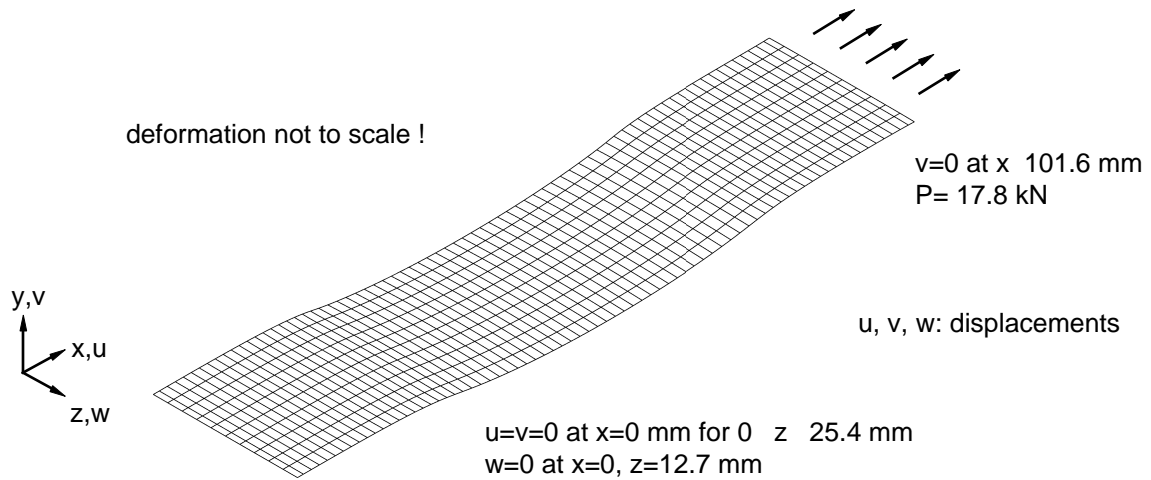


(c). Outline of submodel with discretely modeled damage.

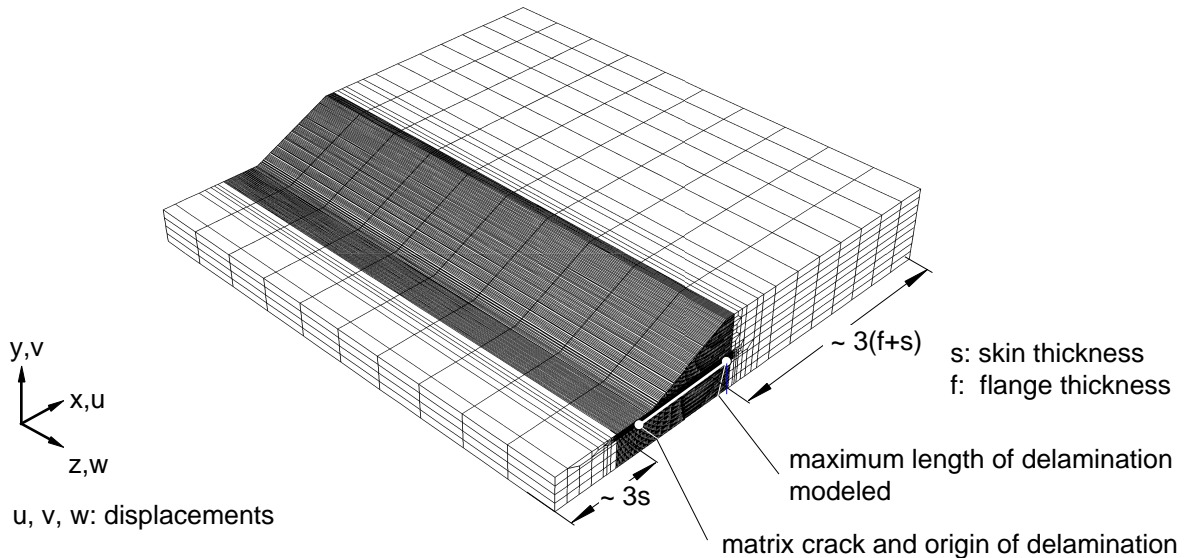
Figure 8. Submodelling technique using a global model made of shell elements.



(a). Deformed global shell model of bending specimen with load and boundary conditions.

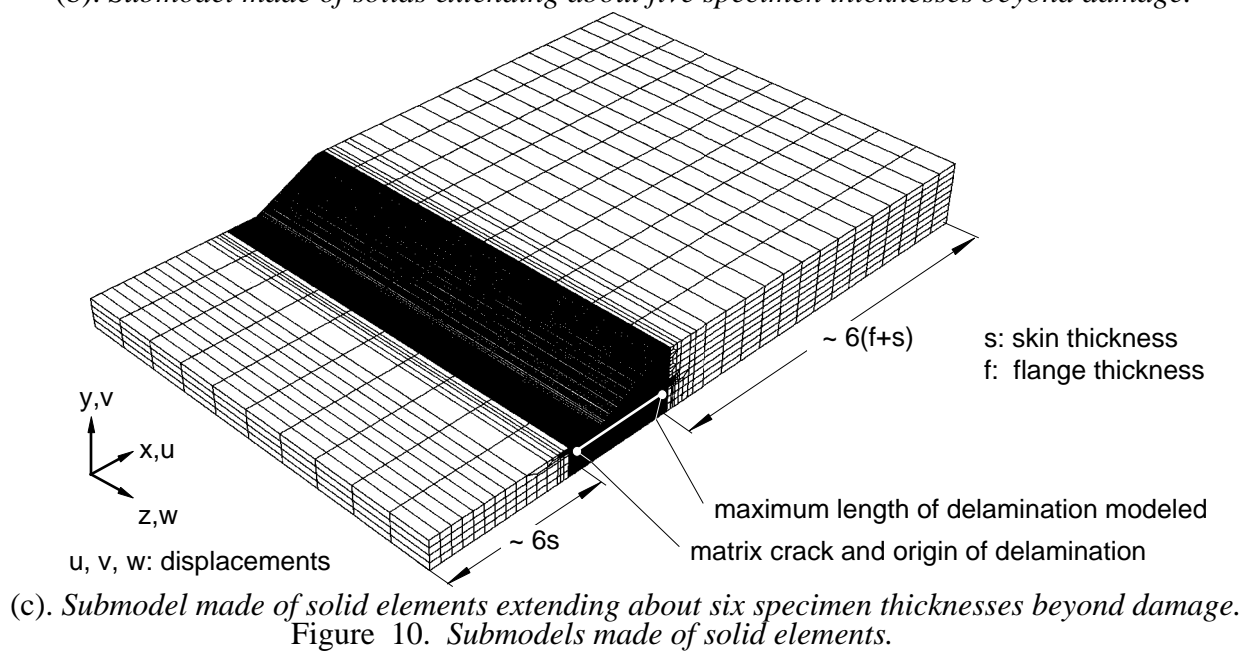
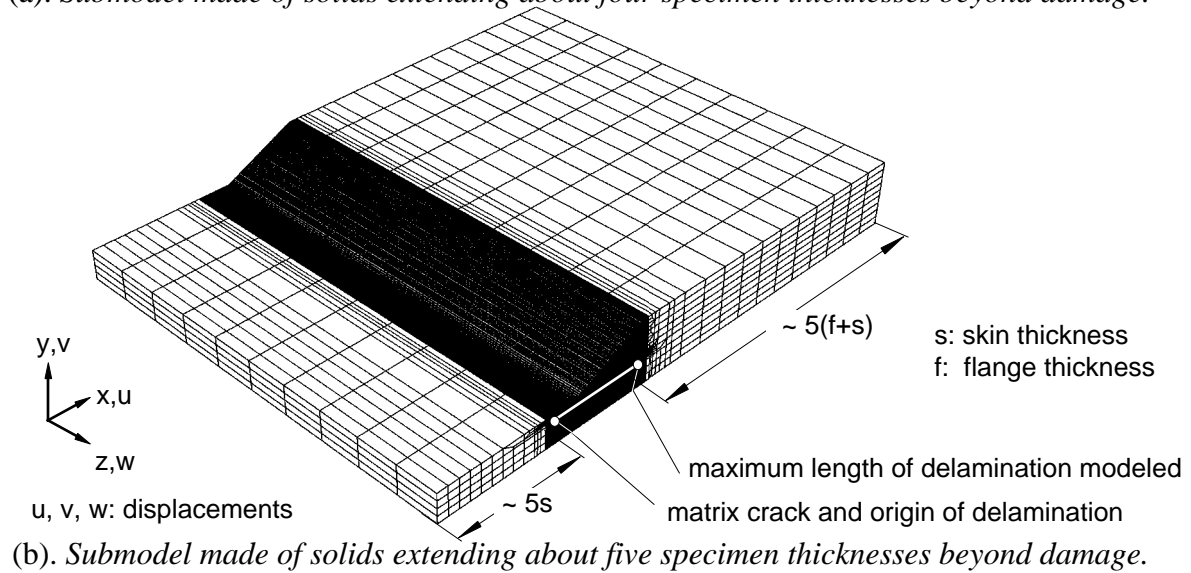
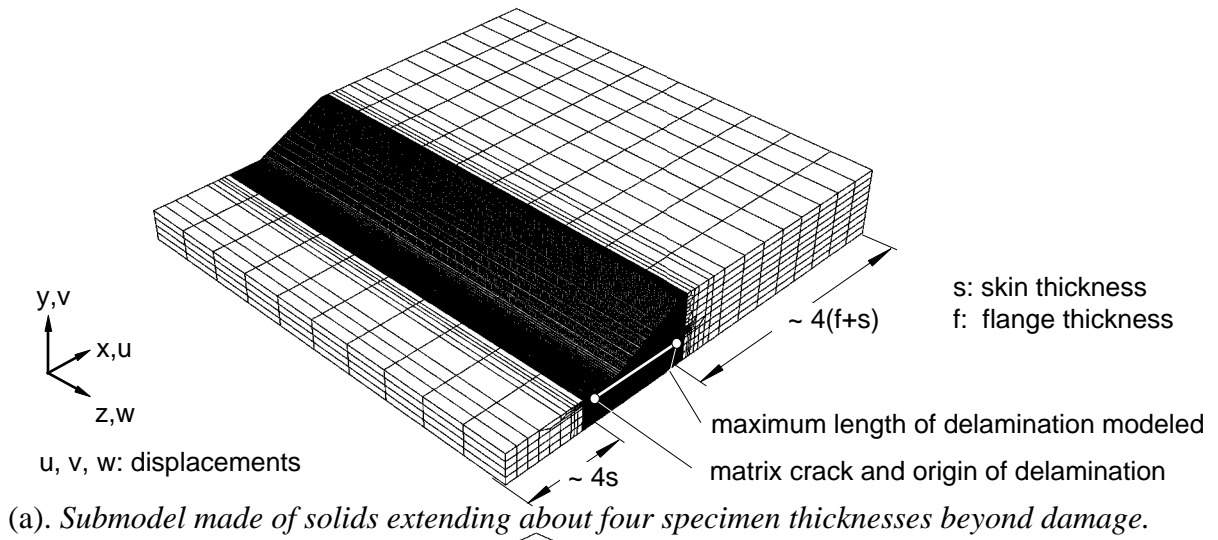


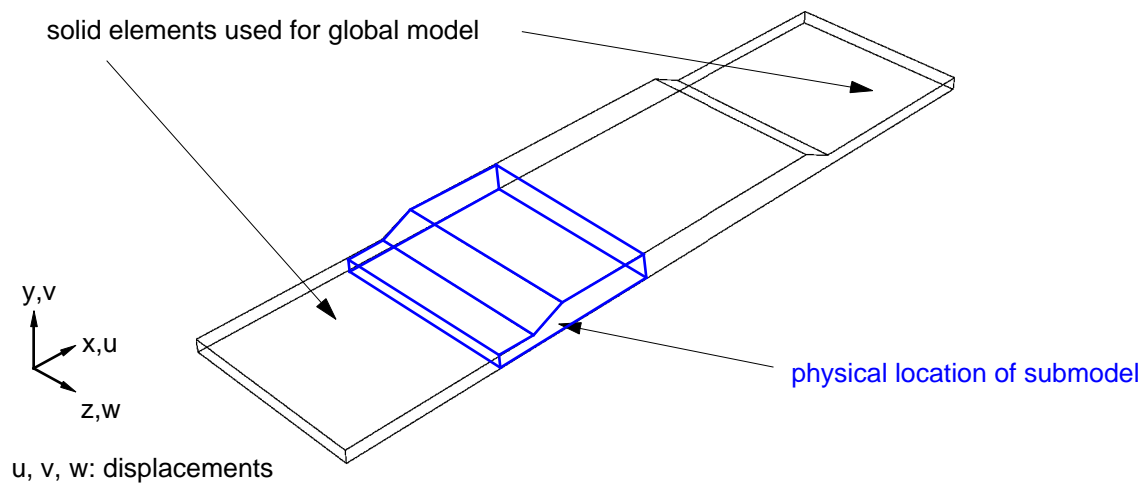
(b). Deformed global shell model of tension specimen with load and boundary conditions



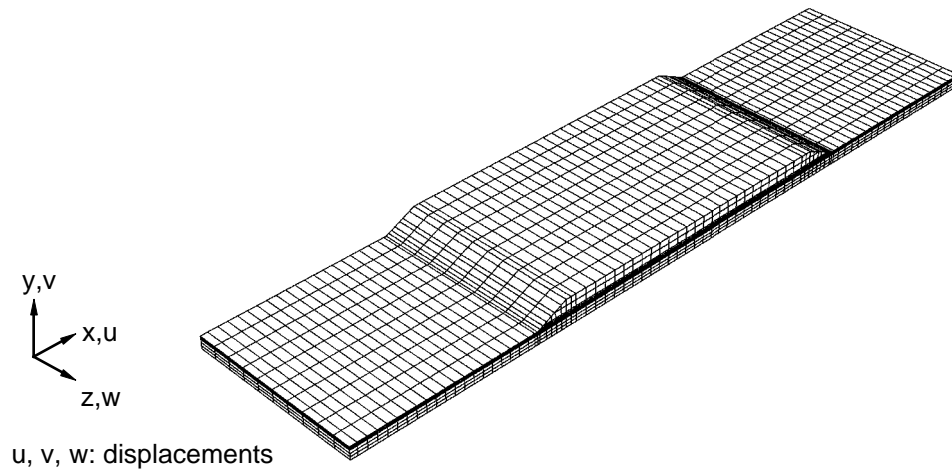
(c). Submodel made of solids extending about three specimen thicknesses beyond damage.

Figure 9. Finite element models used for submodeling technique.

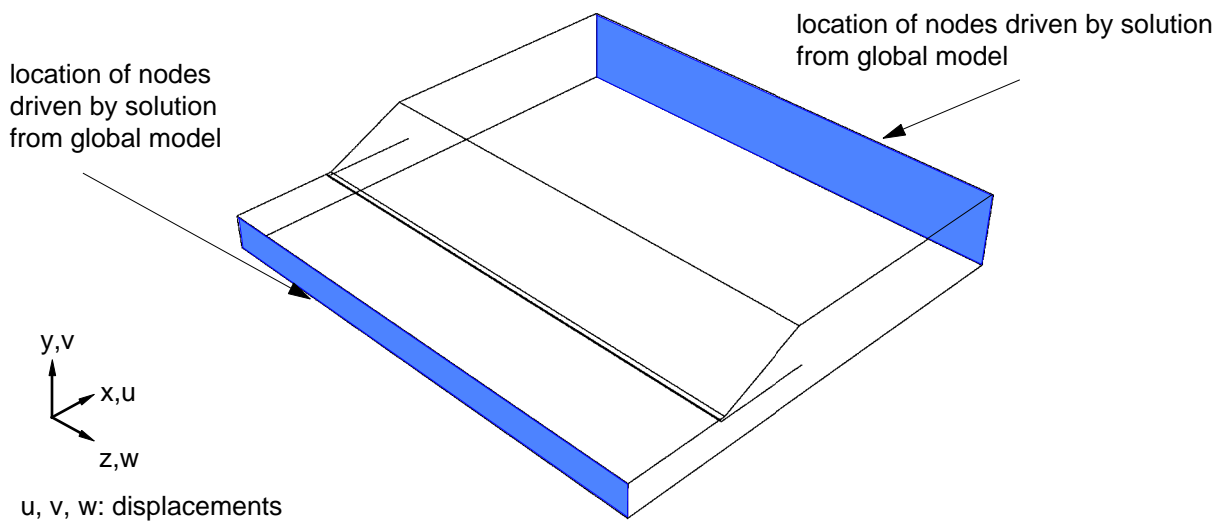




(a). Outline of submodelling technique using solid elements for global model and submodel.



(b). Global model of skin/flange specimen modeled with solid elements.



(c). Outline of submodel with discretely modeled damage.

Figure 11. Submodelling technique using a global model made of solid elements.

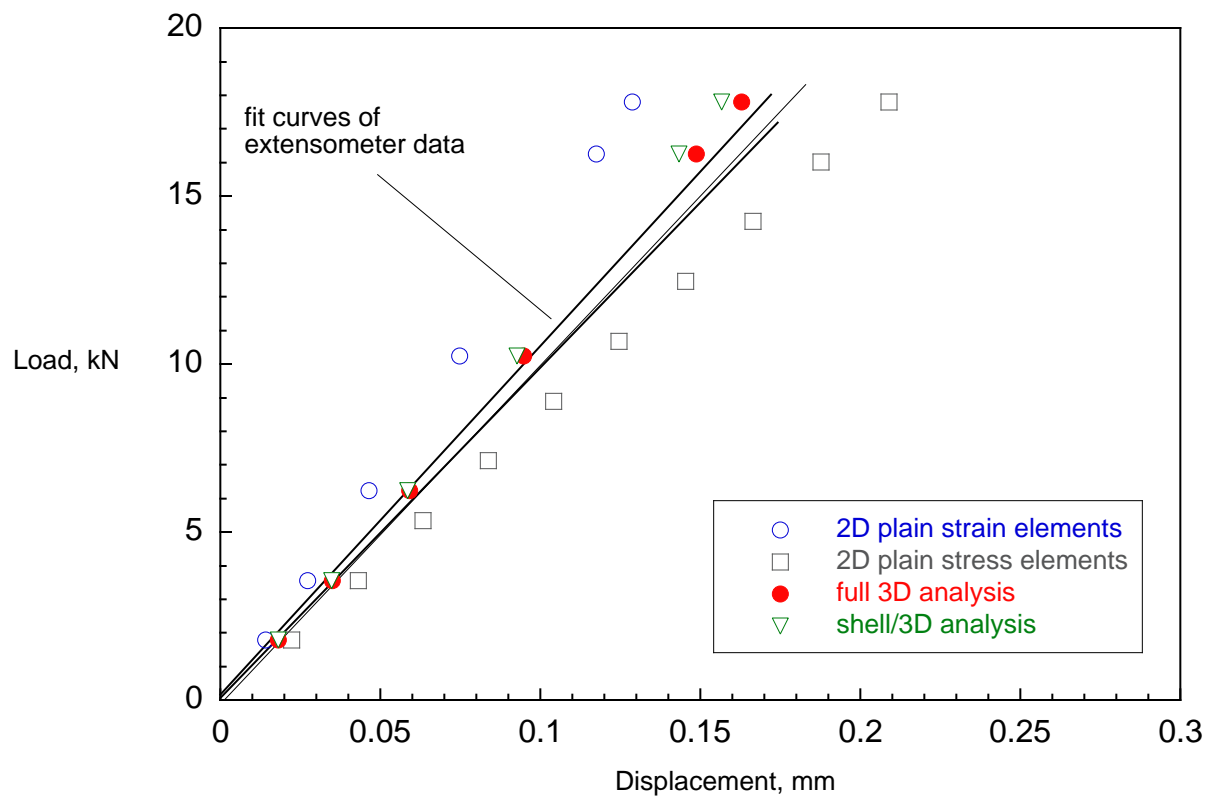


Figure 12. Load-displacement plots for tension tests.

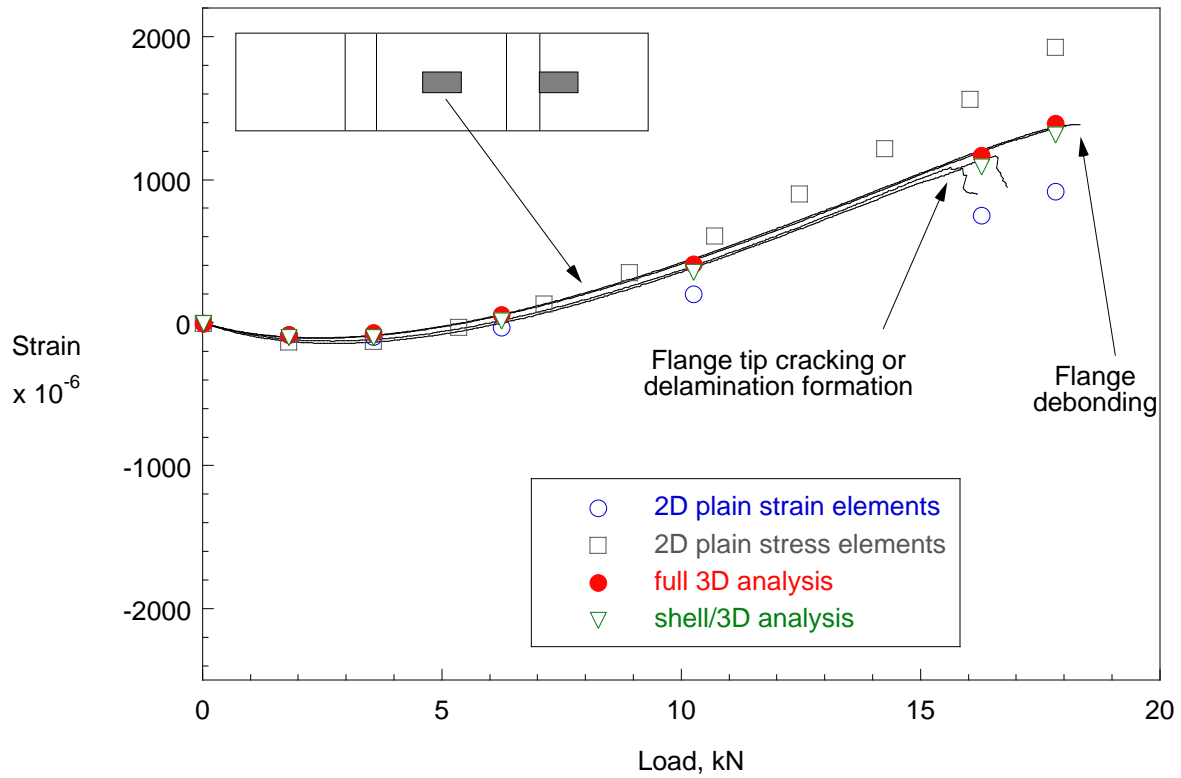


Figure 13. *Flange strain-load plots for tension tests.*

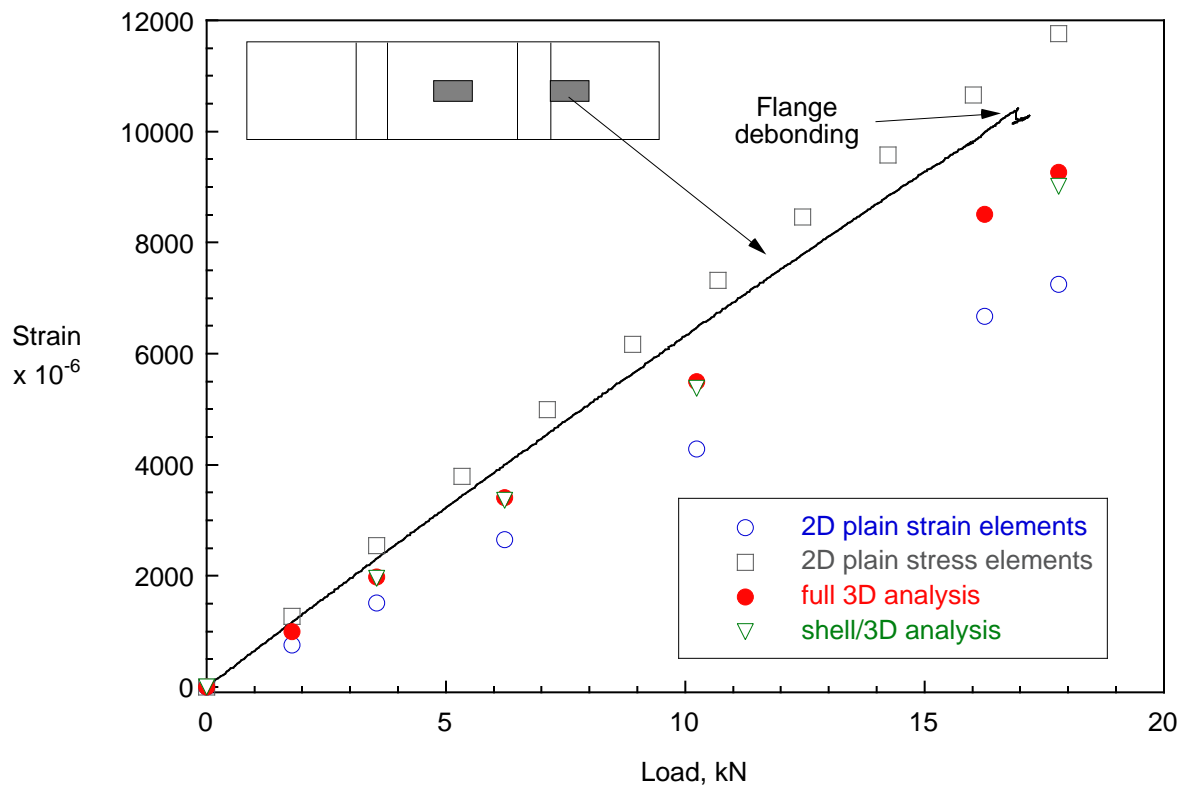
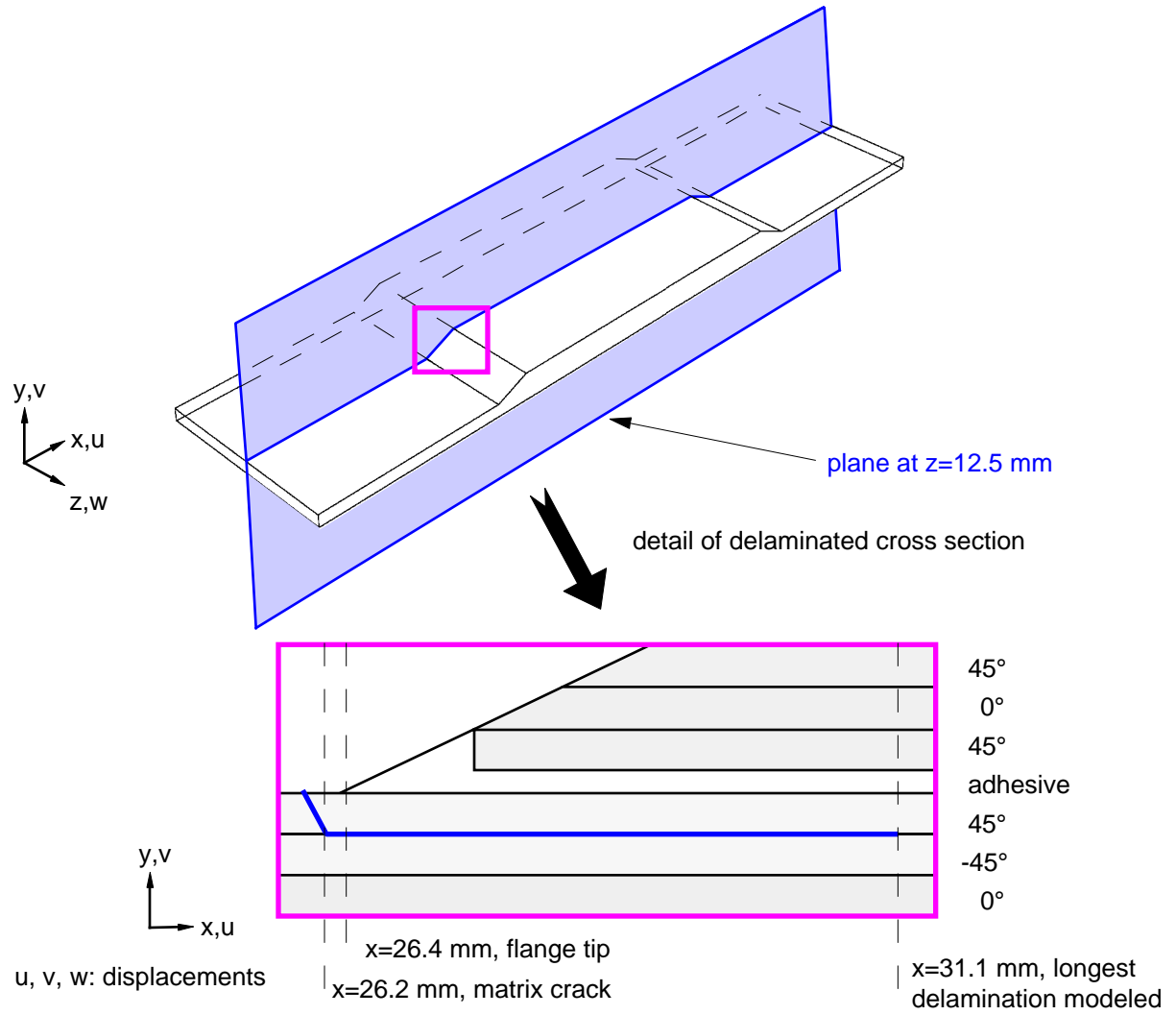
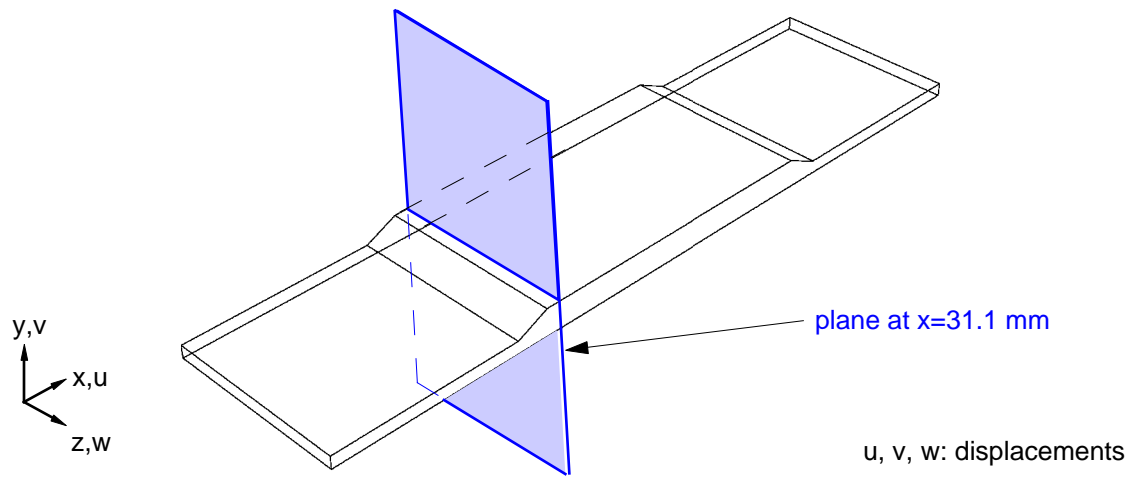


Figure 14. *Typical skin strain-load plot for tension tests.*



(a). XY-plane at $z=12.5$ mm for display of results along the length in the center of the specimen.



(b). YZ-plane at $x=31.1$ mm for display of results across the width of the specimen.

Figure 15. Section planes through the specimen

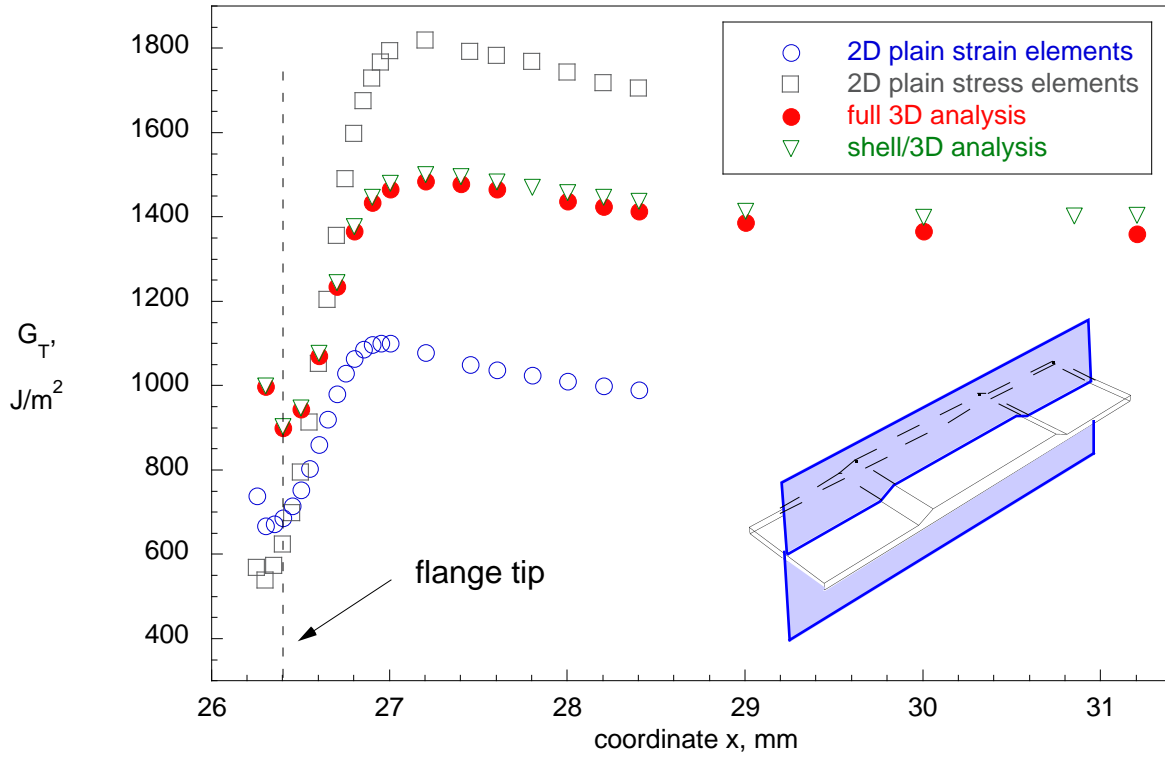


Figure 16. *Computed total energy release rate for delamination growing from matrix crack in skin top 45°/-45°ply interface for tension test.*

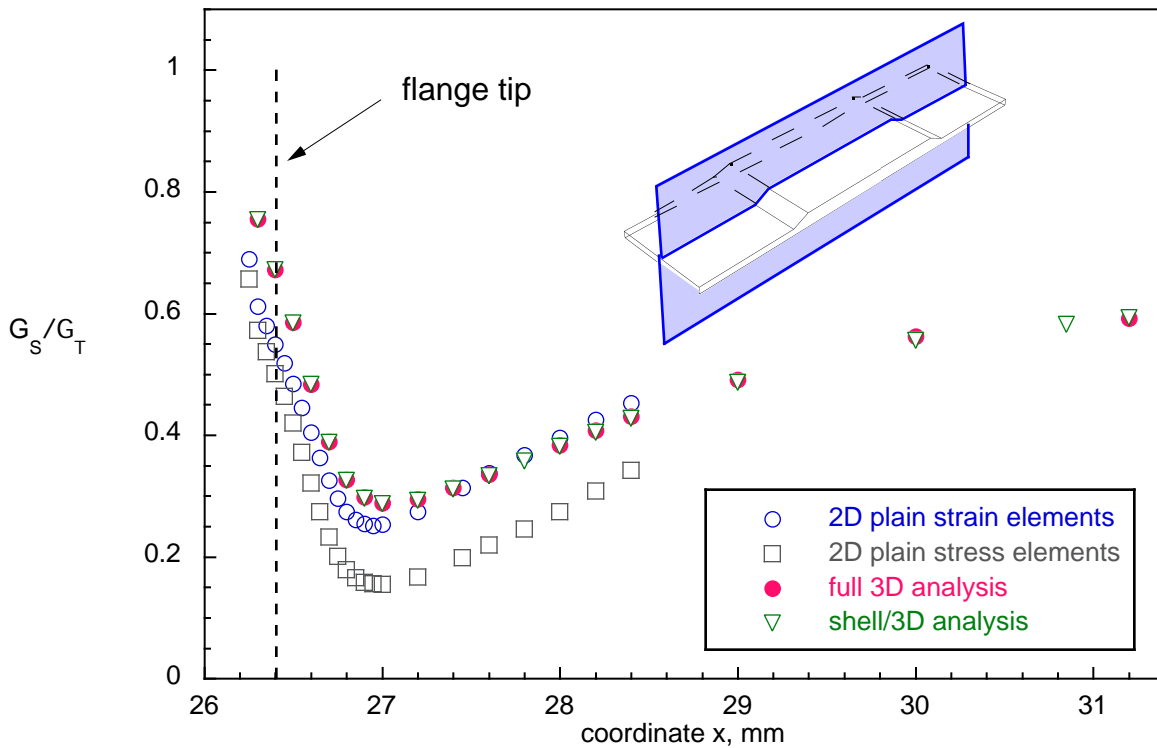


Figure 17. *Computed mixed mode ratio G_S/G_T for delamination growing from matrix crack in skin top 45°/-45°ply interface for tension test.*

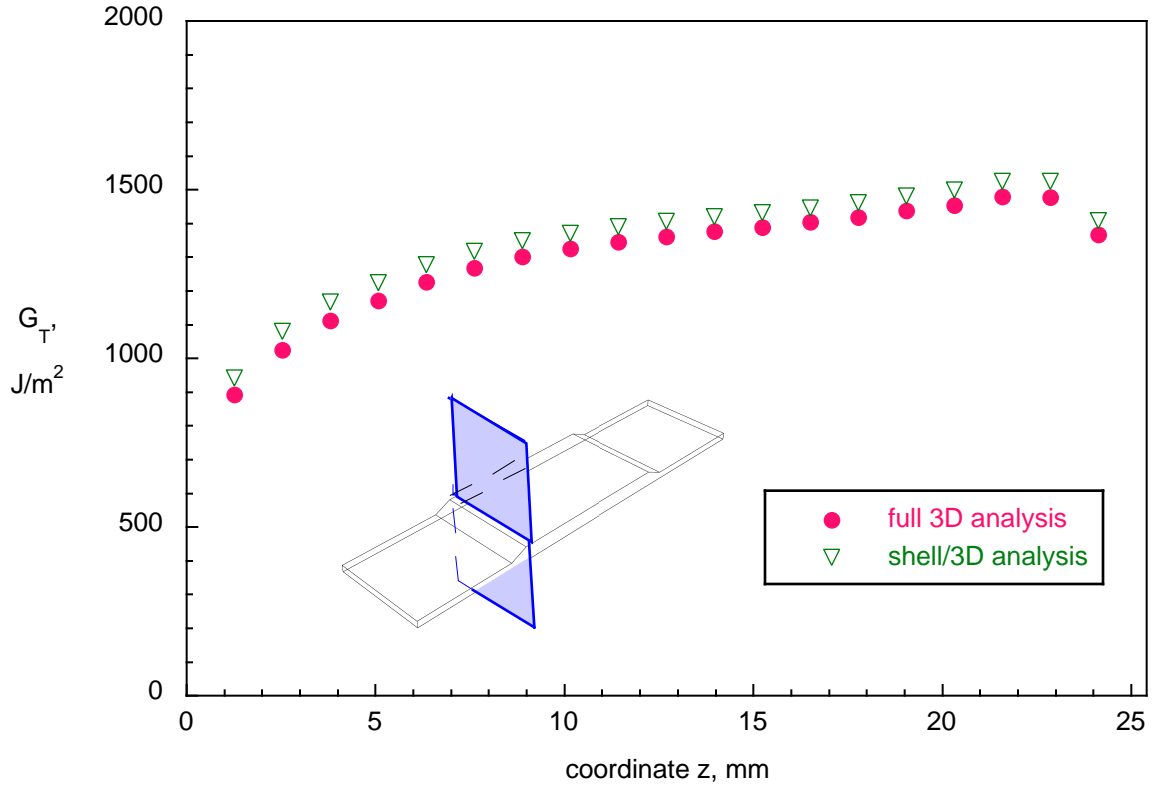


Figure18. Computed total energy release rate across the width of the specimen at $x= 31.2$ mm for tension test (coarse mesh).

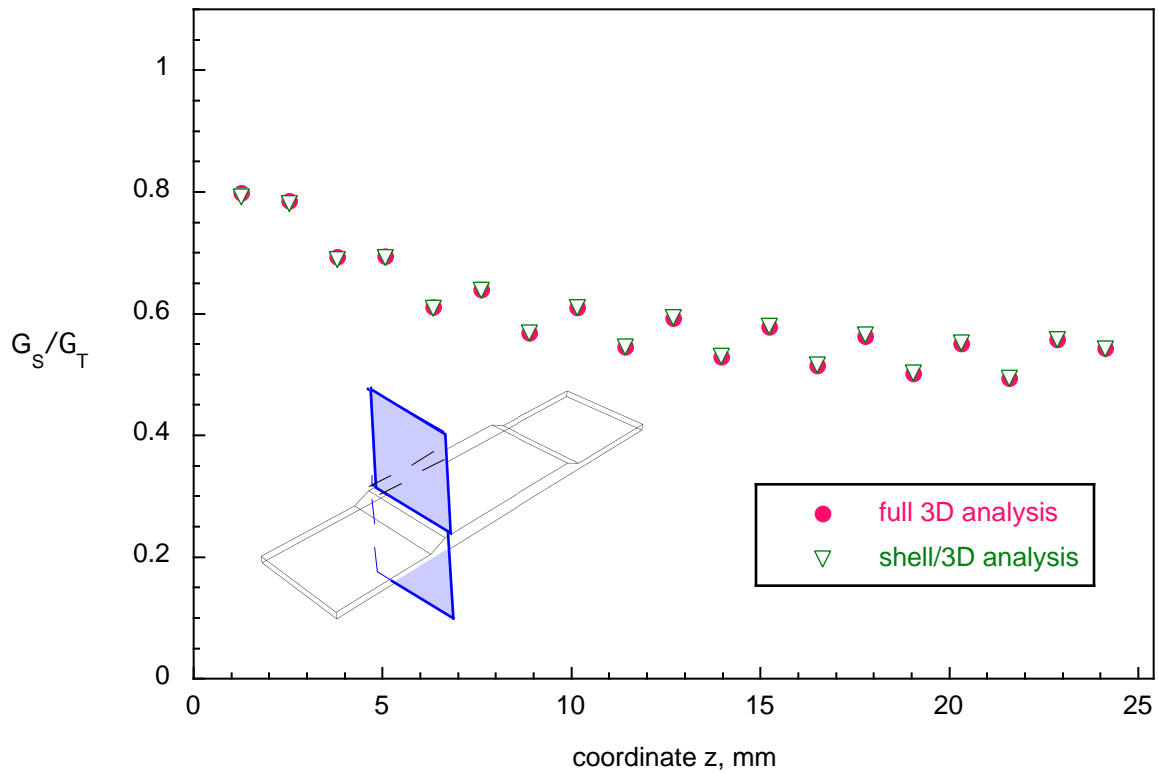


Figure 19. Computed mixed mode ratio across the width of the specimen at $x= 31.2$ mm for tension test (coarse mesh).

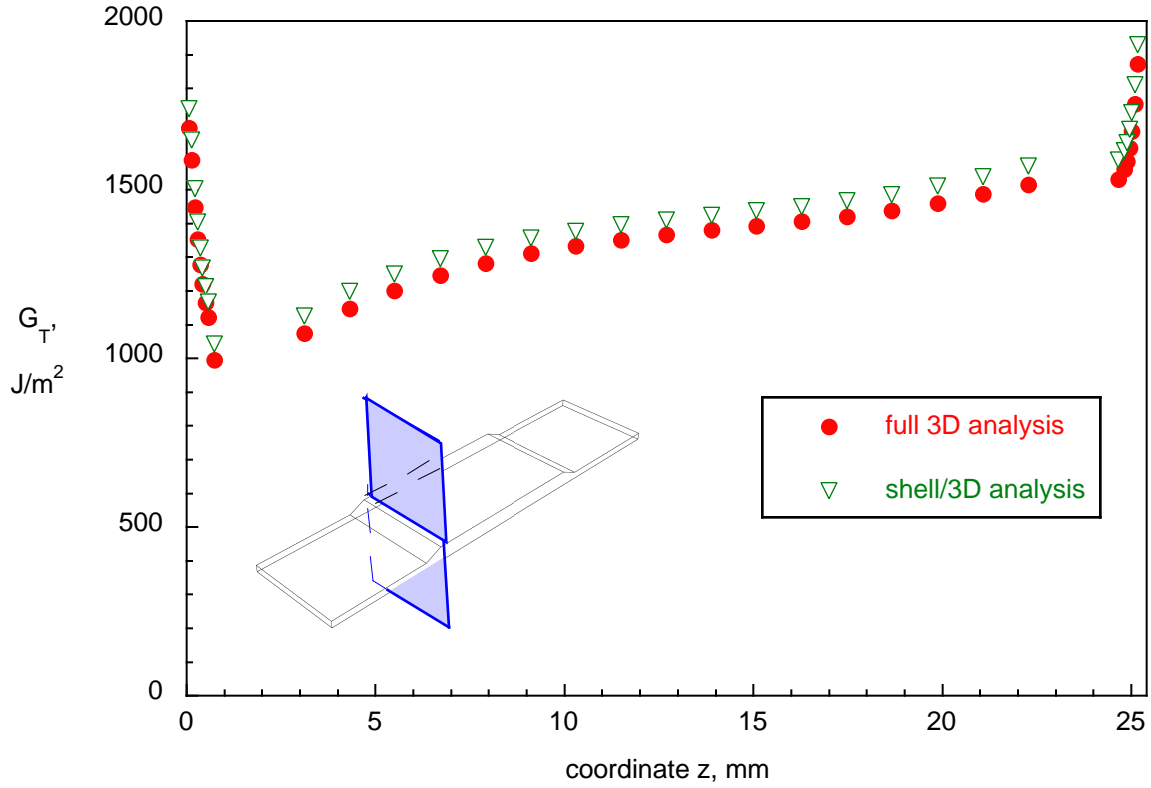


Figure 20. Computed total energy release rate across the width of the specimen at $x= 31.2$ mm for tension test (refined mesh).

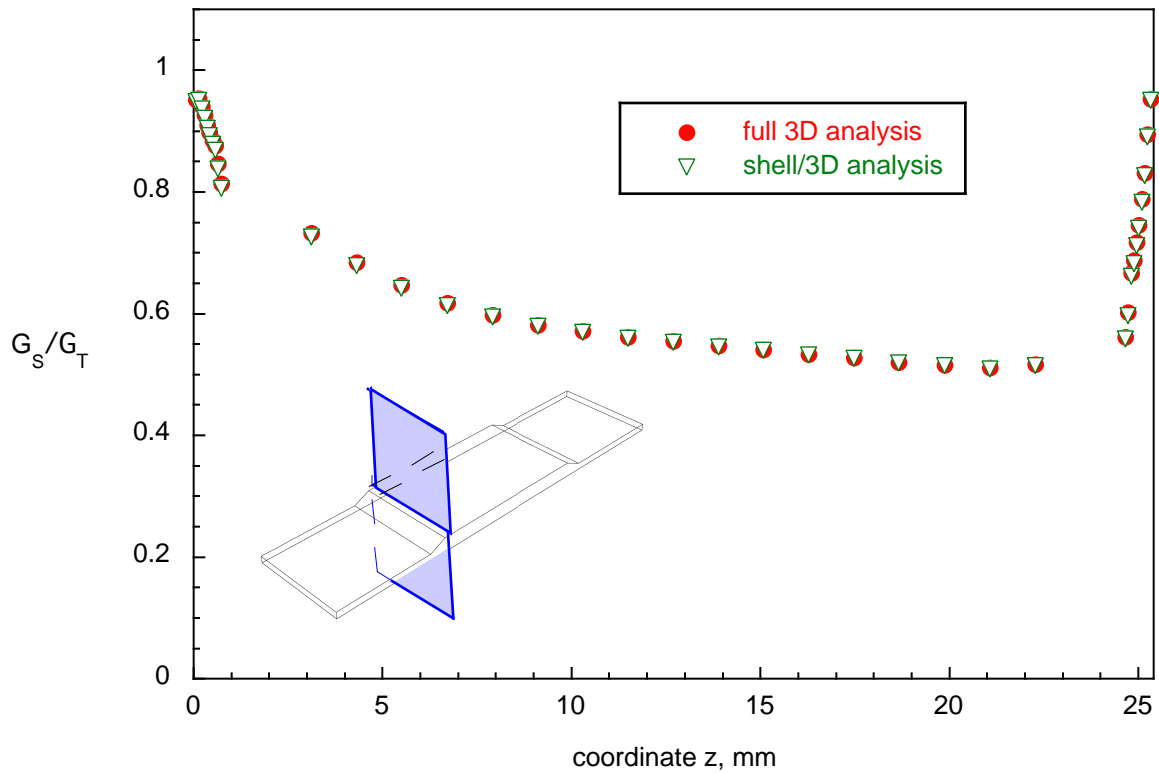


Figure 21. Computed mixed-mode ratio across the width of the specimen at $x= 31.2$ mm for tension test (refined mesh).

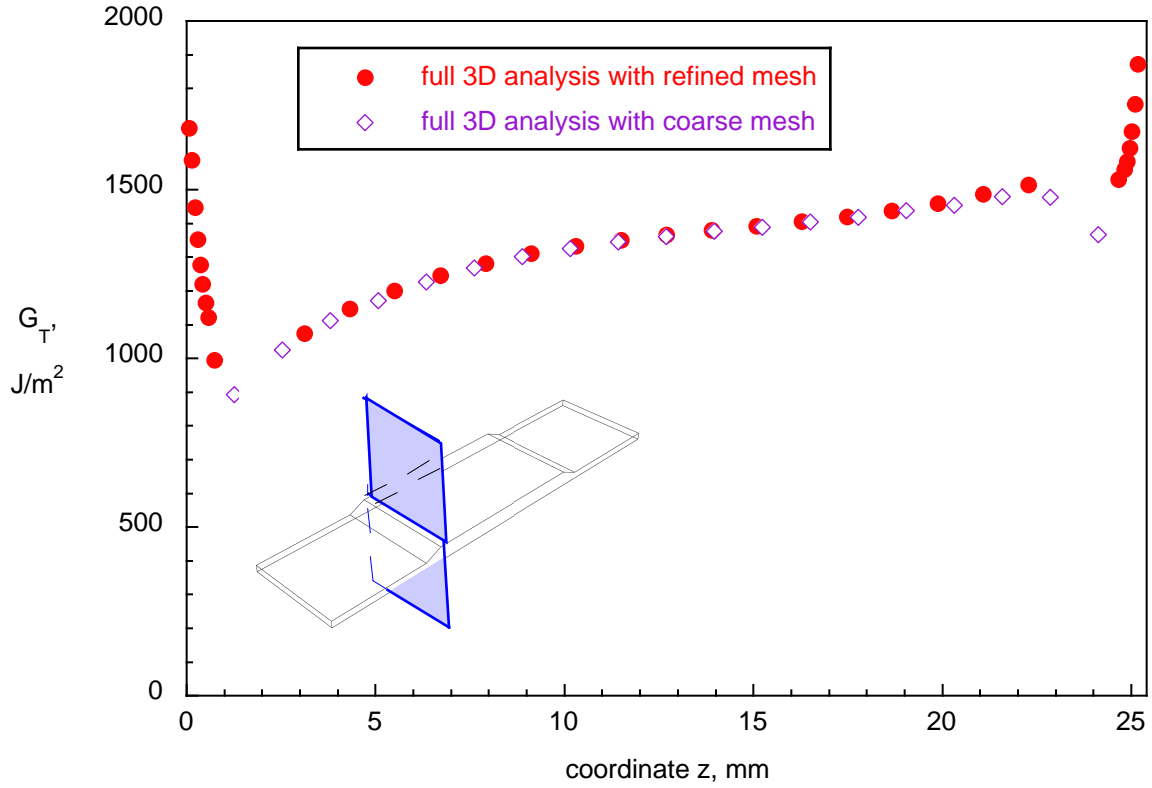


Figure 22. Computed total energy release rate across the width of the specimen at $x = 31.2$ mm for tension test (full 3D analysis).

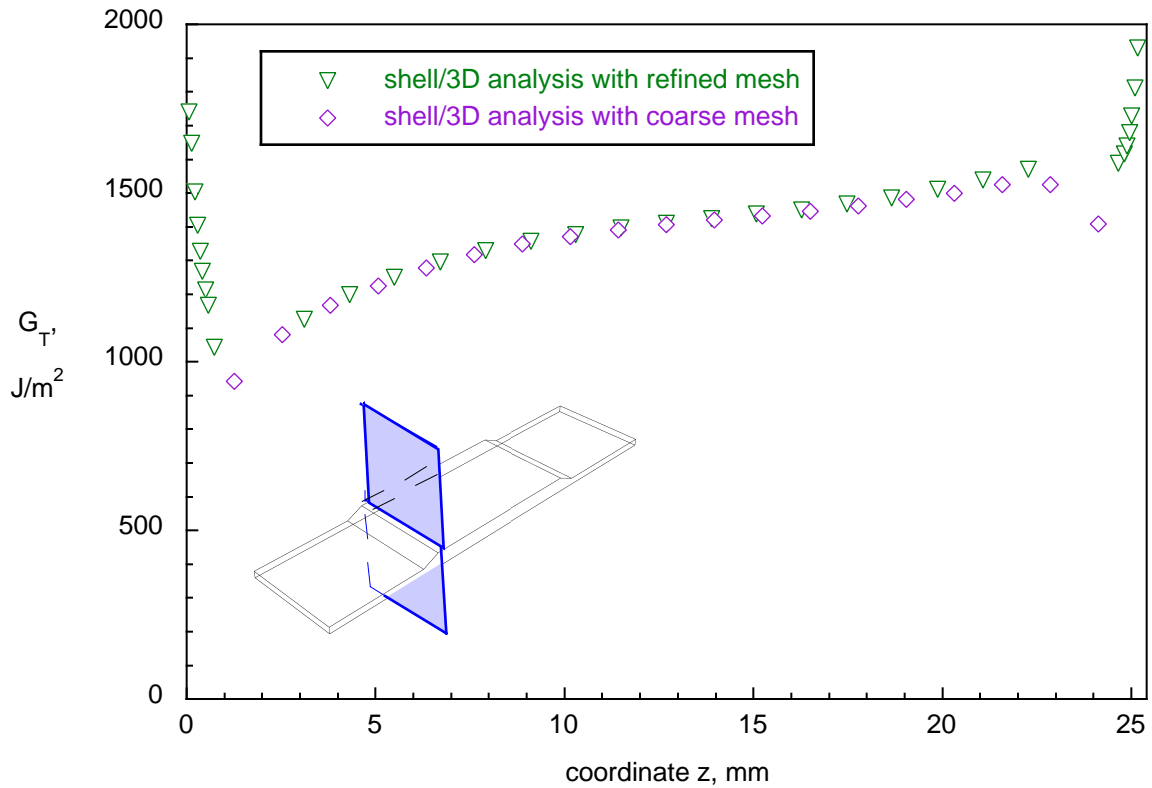


Figure 23. Computed total energy release rate across the width of the specimen at $x = 31.2$ mm for tension test (shell/3D analysis).

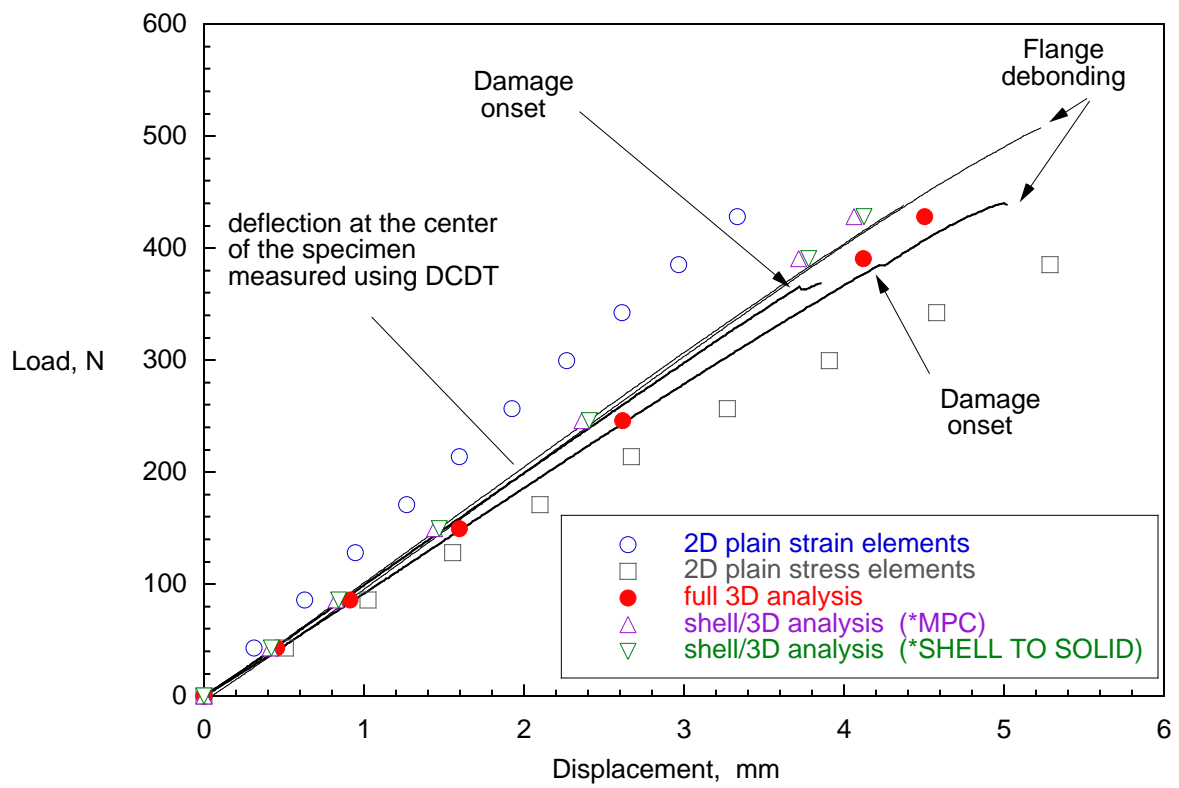


Figure 24. Load-displacement plots for three-point bending tests.

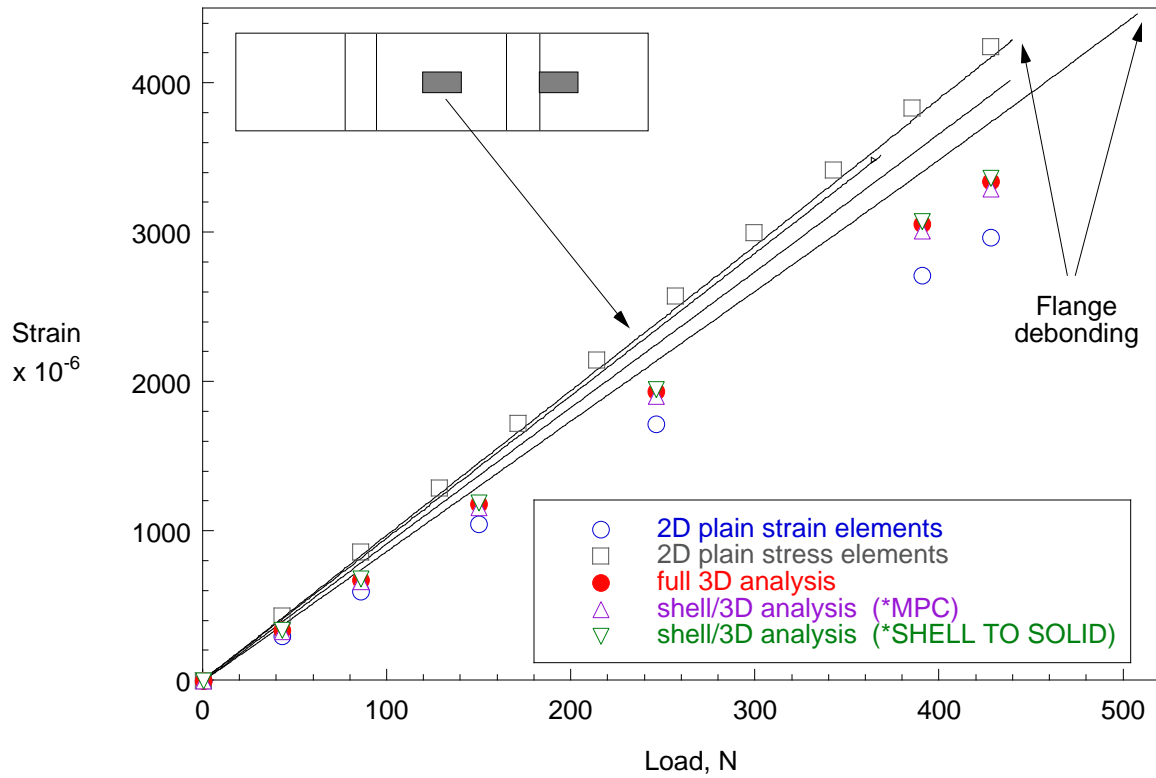


Figure 25. *Flange strain-load plots for three-point bending tests.*

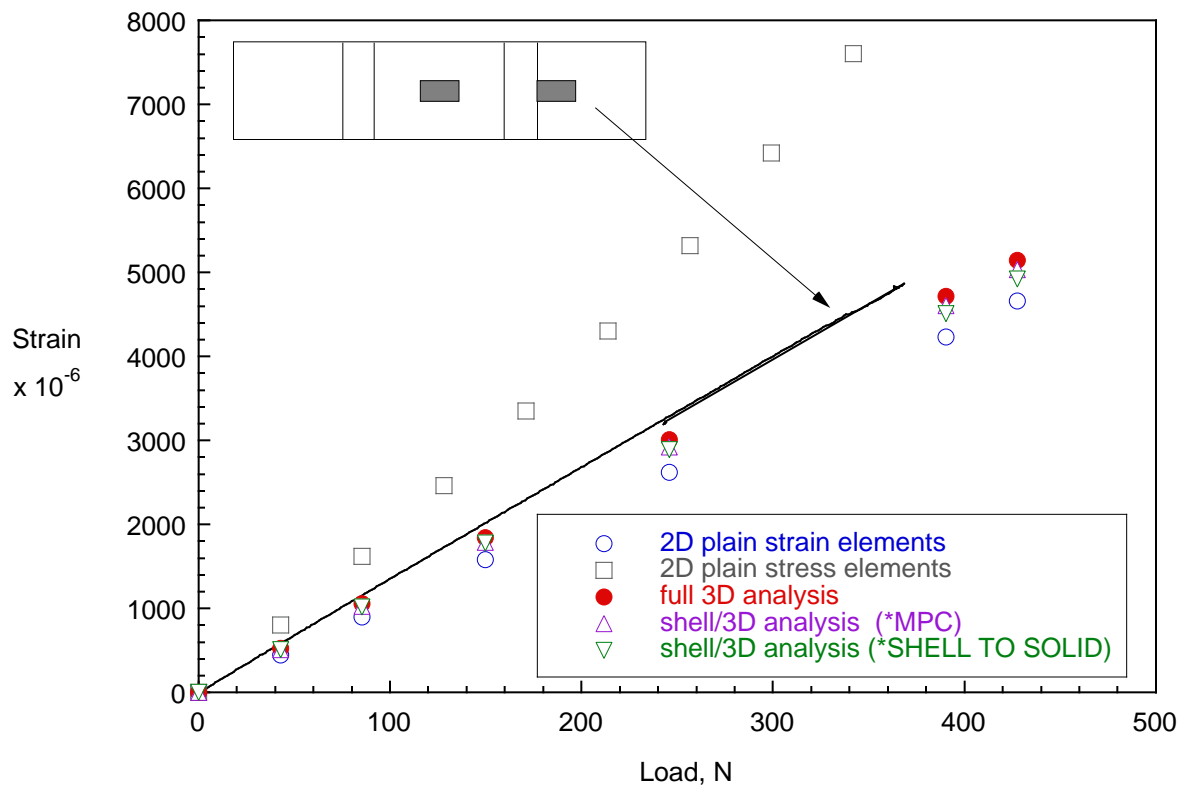


Figure 26. *Skin strain-load plot for three-point bending tests.*

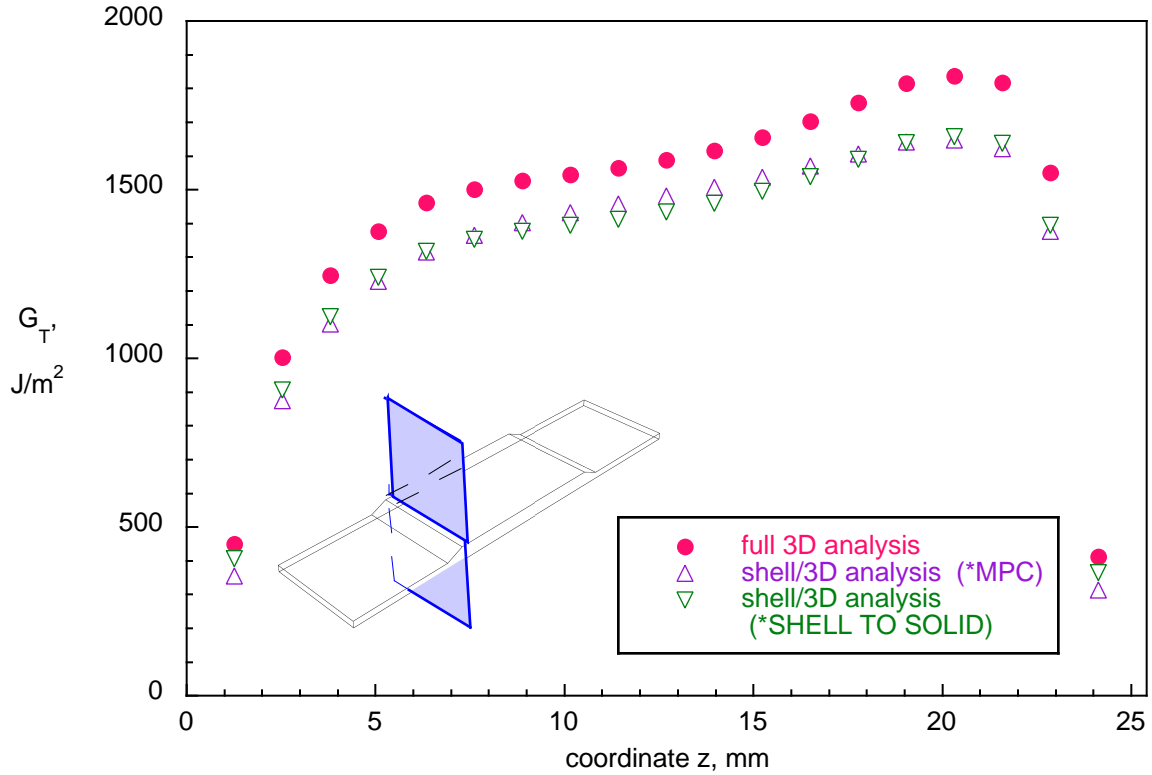


Figure 27. Computed total energy release rate across the width of the specimen at $x = 31.2$ mm for three-point bending test (coarse mesh).

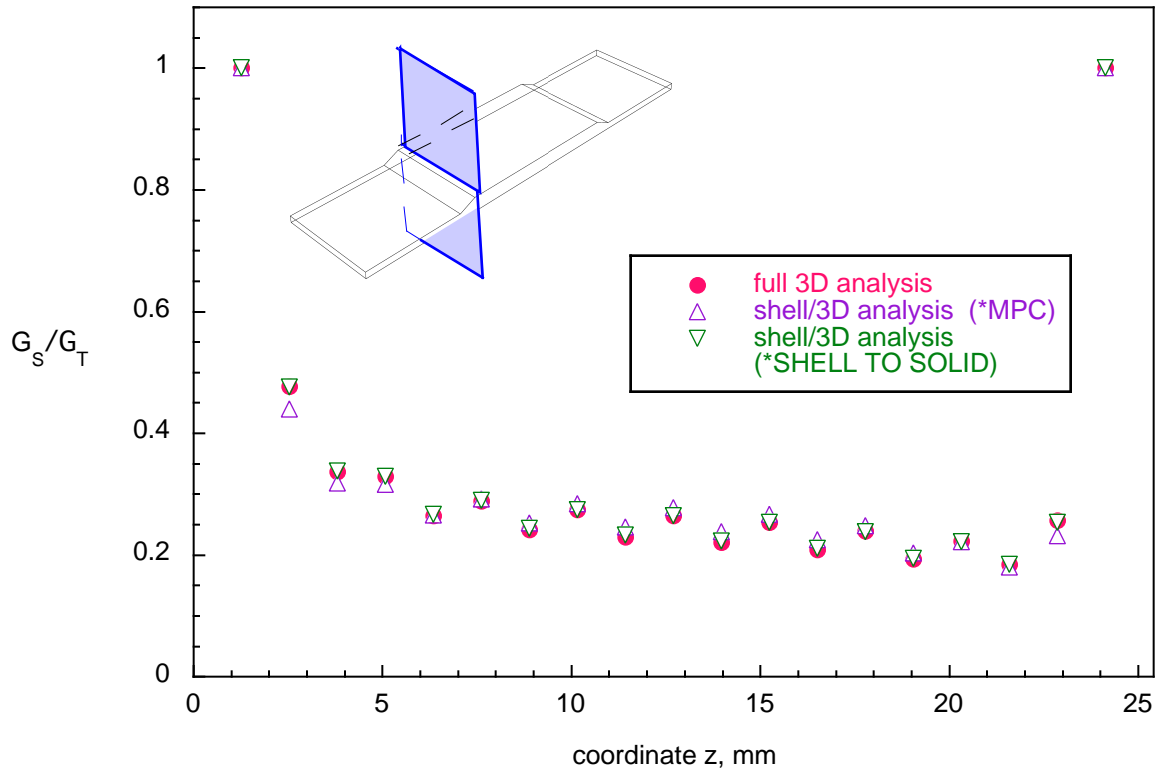


Figure 28. Computed mixed mode ratio across the width of the specimen at $x = 31.2$ mm for three-point bending test (coarse mesh).

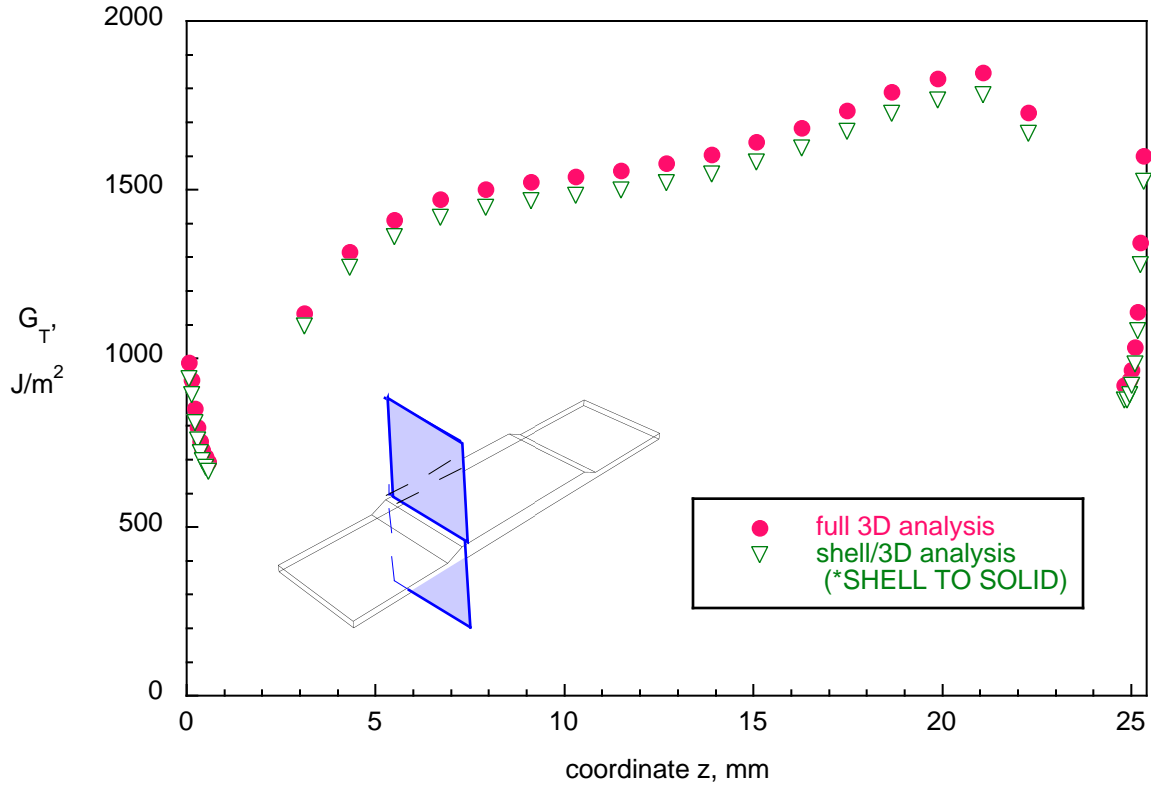


Figure 29. Computed total energy release rate across the width of the specimen at $x = 31.2$ mm for three-point bending test (refined mesh).

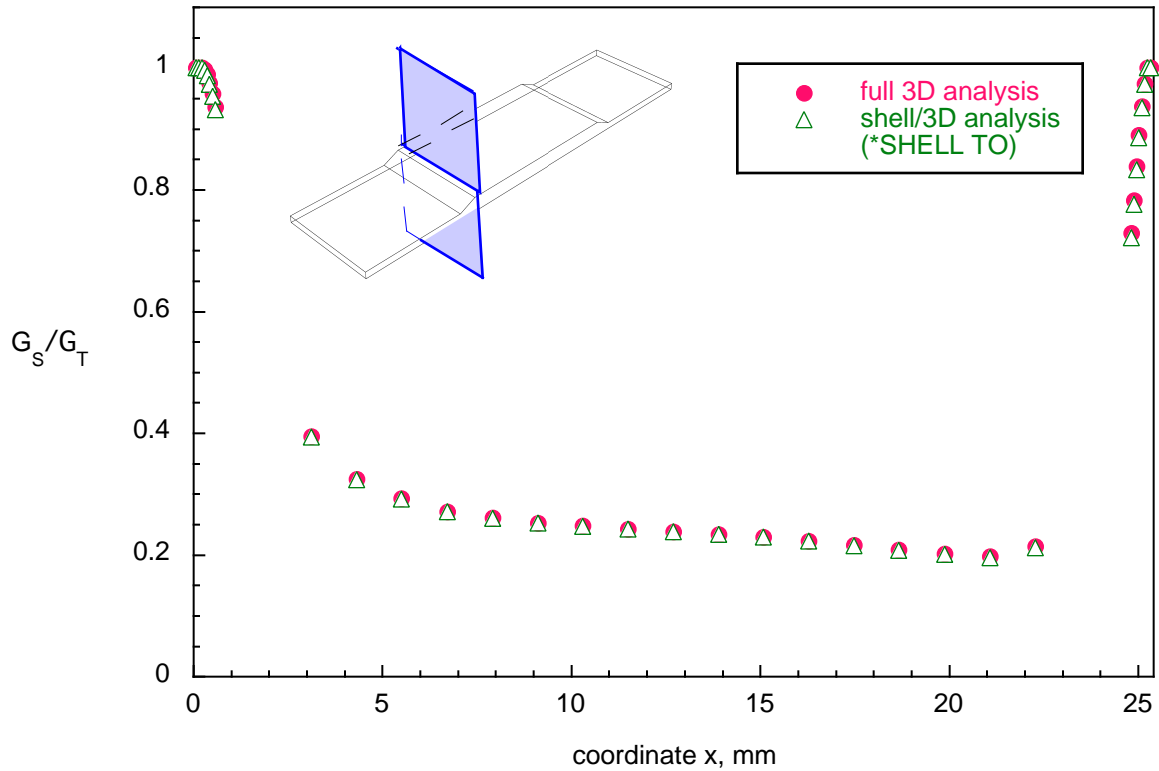


Figure 30. Computed mixed mode ratio across the width of the specimen at $x = 31.2$ mm for three-point bending test (refined mesh).

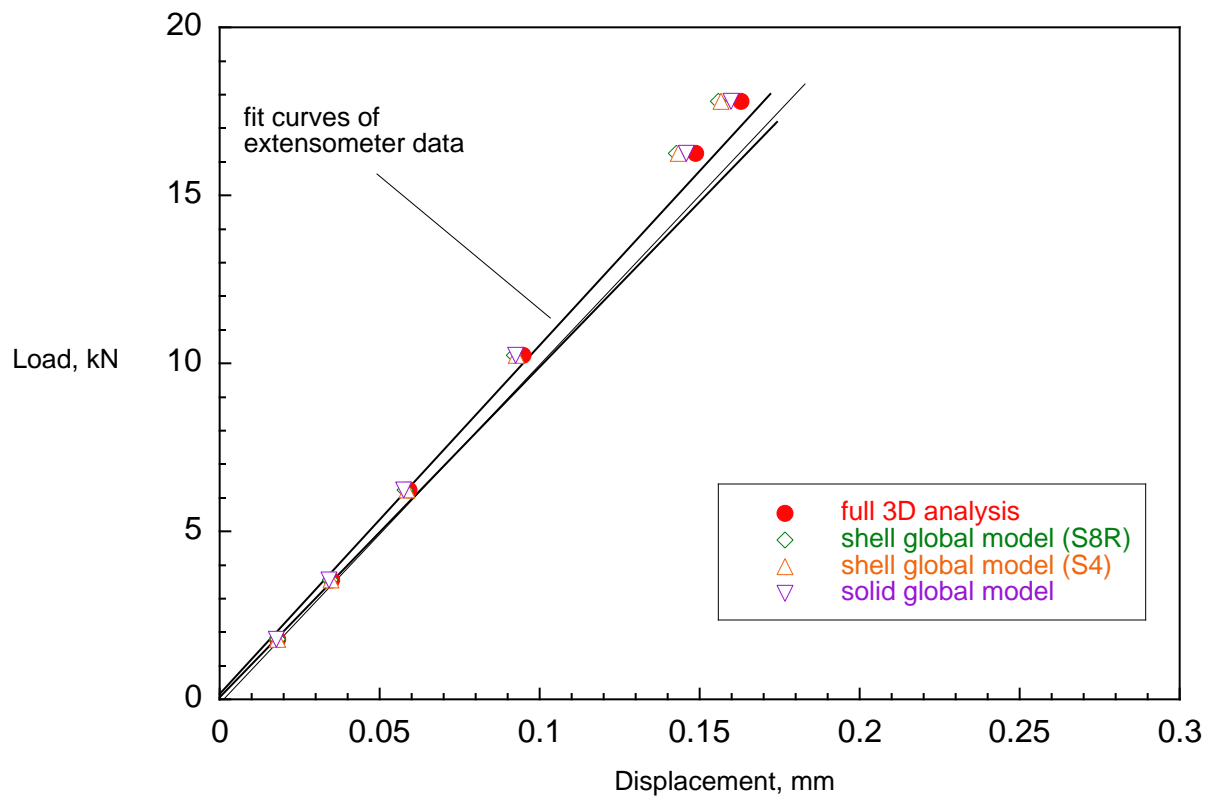


Figure 31. Load-displacement plots for tension tests.

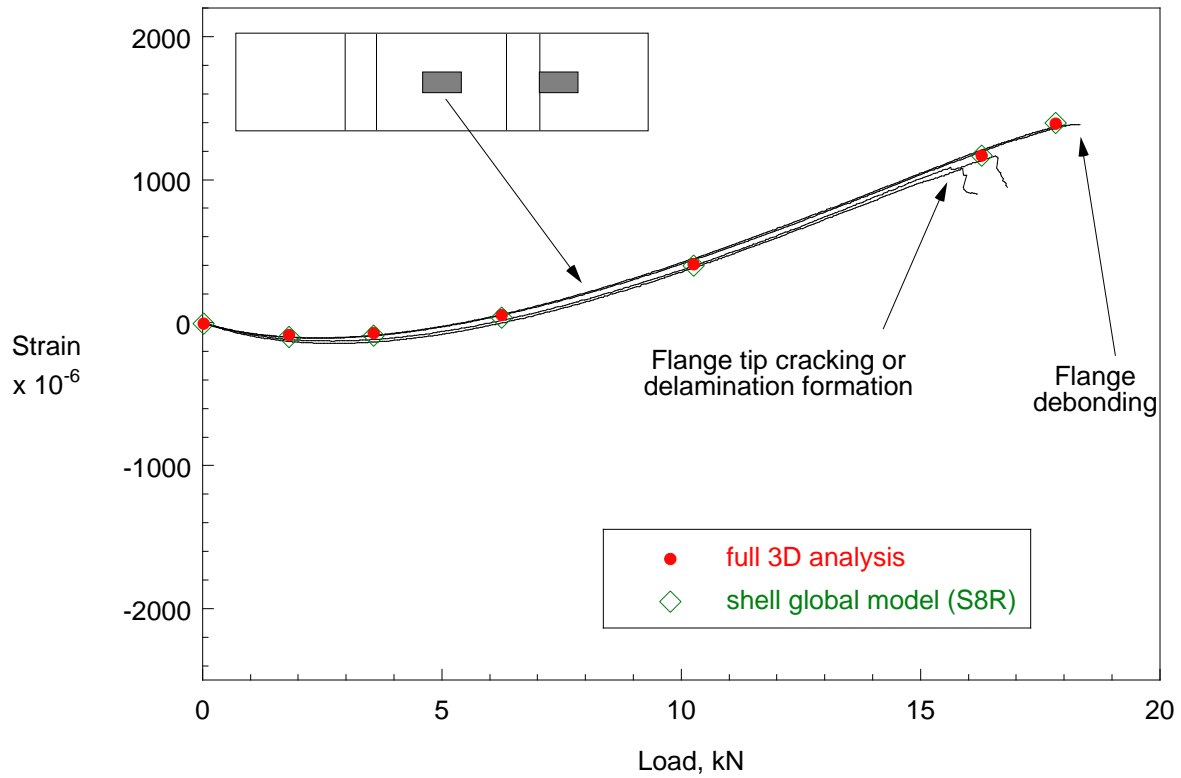


Figure 32. Flange strain-load plots for tension tests.

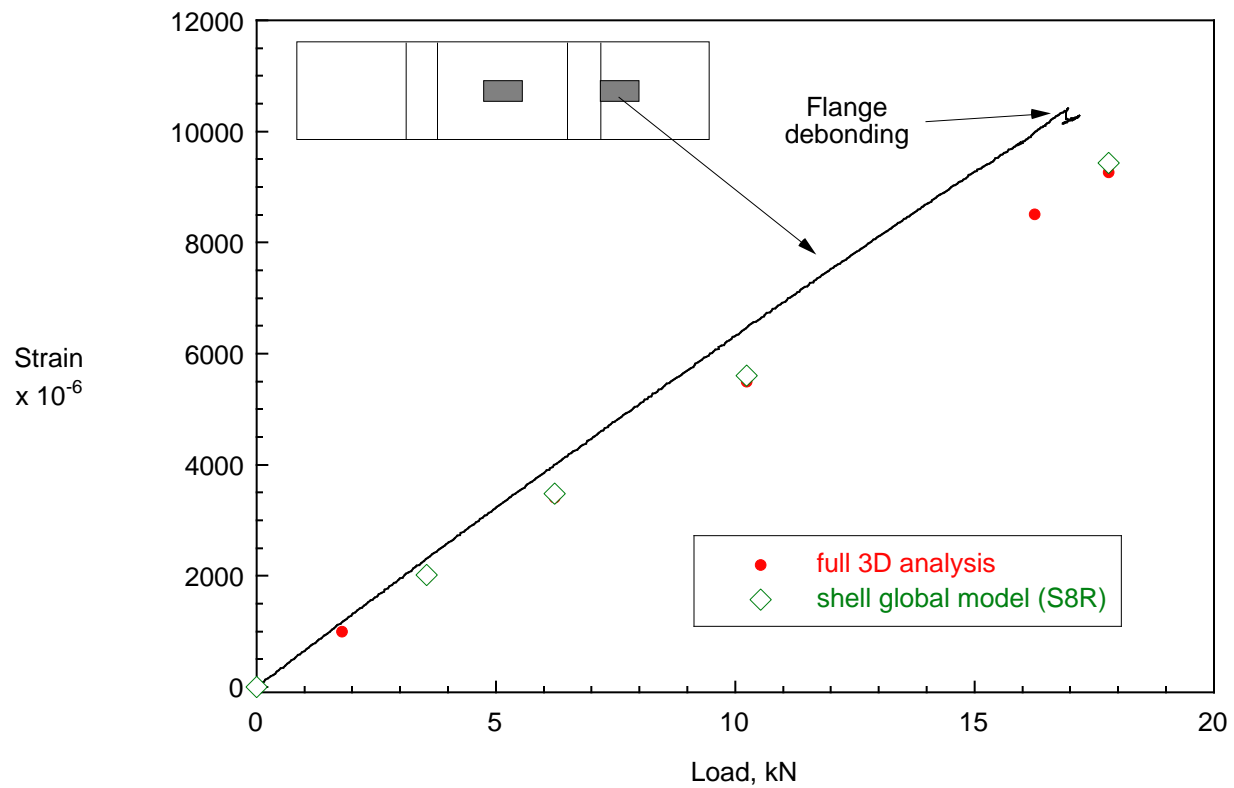


Figure 33. Typical skin strain-load plot for tension tests.

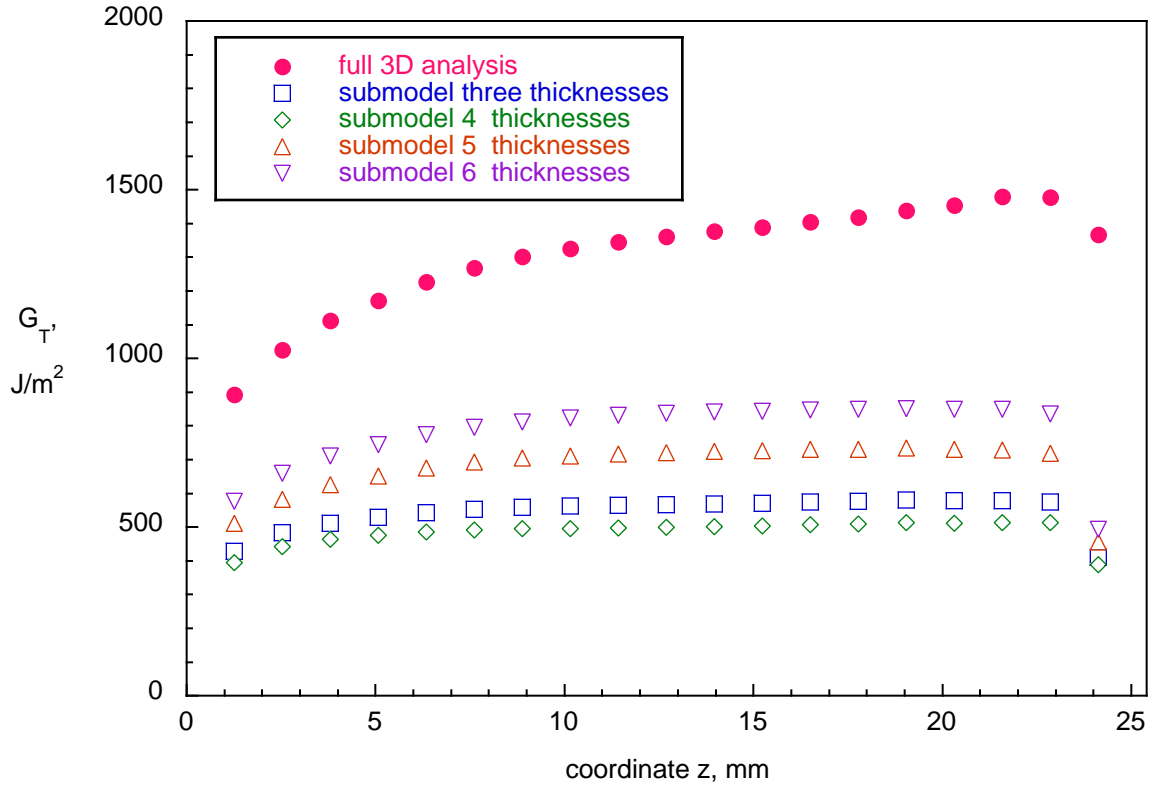


Figure 34. Computed total energy release rate across the width of the specimen at $x = 31.2$ mm for tension test.

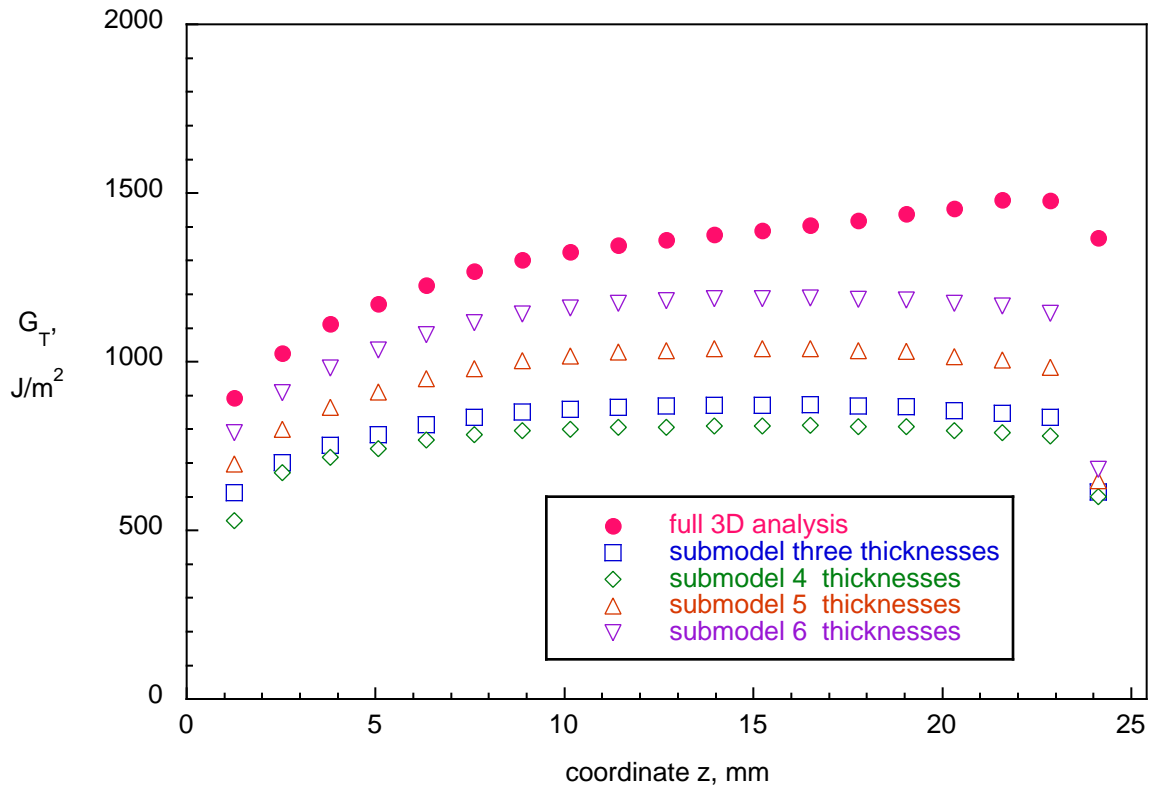


Figure 35. Computed total energy release rate across the width of the specimen at $x = 31.2$ mm for tension test.

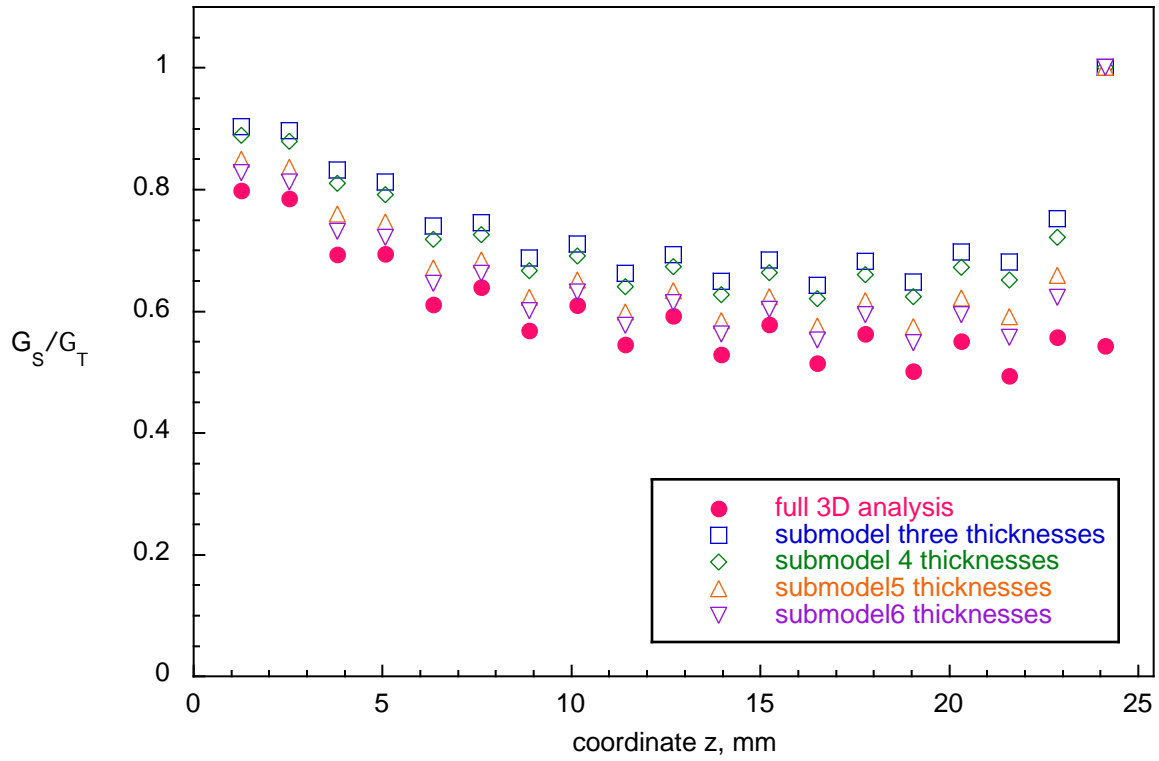


Figure 36. Computed mixed mode ratio across the width of the specimen at $x = 31.2$ mm for tension test.

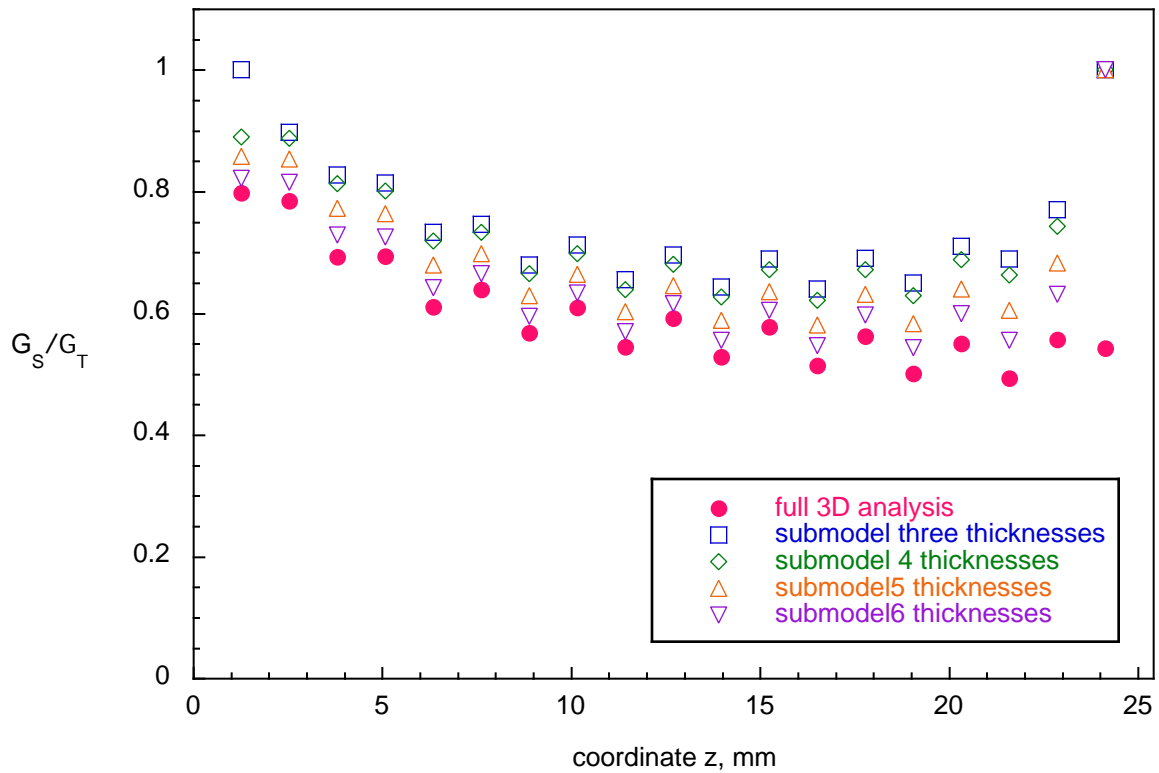


Figure 37. Computed mixed mode ratio across the width of the specimen at $x = 31.2$ mm for tension test.

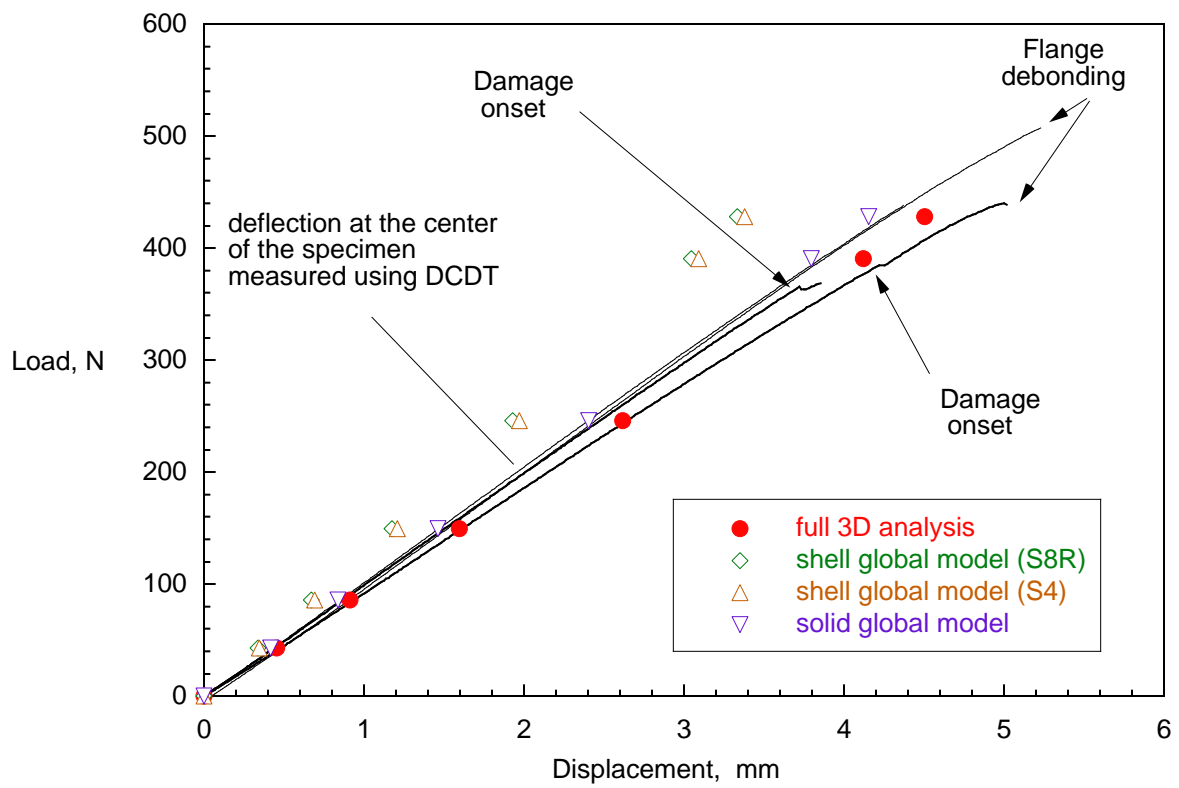


Figure 38. Load-displacement plots for three-point bending tests.

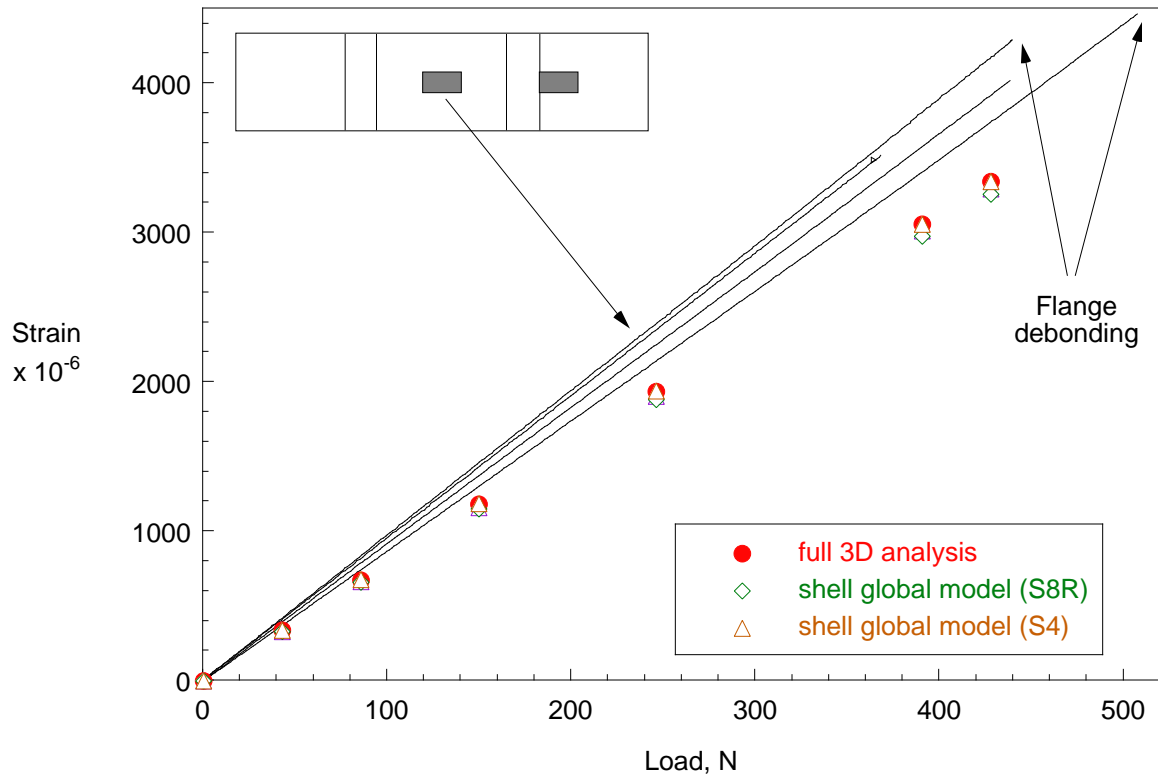


Figure 39. Flange strain-load plots for three-point bending tests.

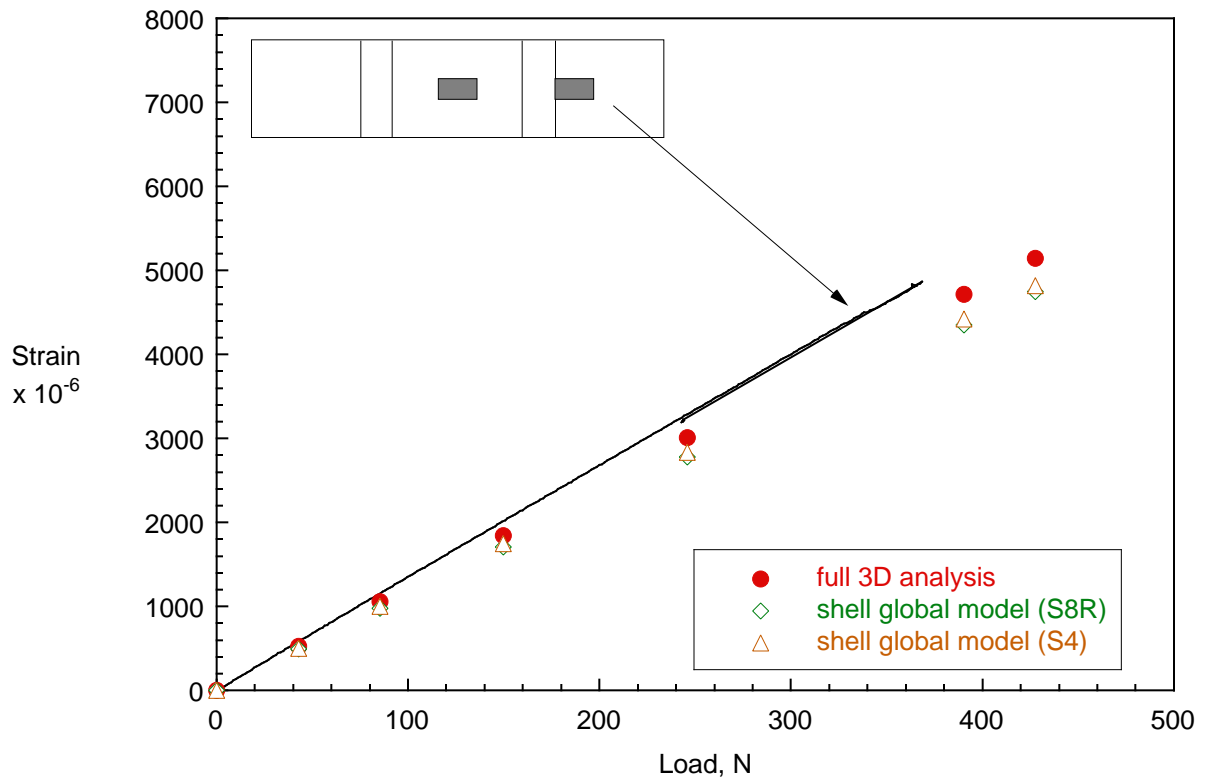


Figure 40. Skin strain-load plot for three-point bending tests.

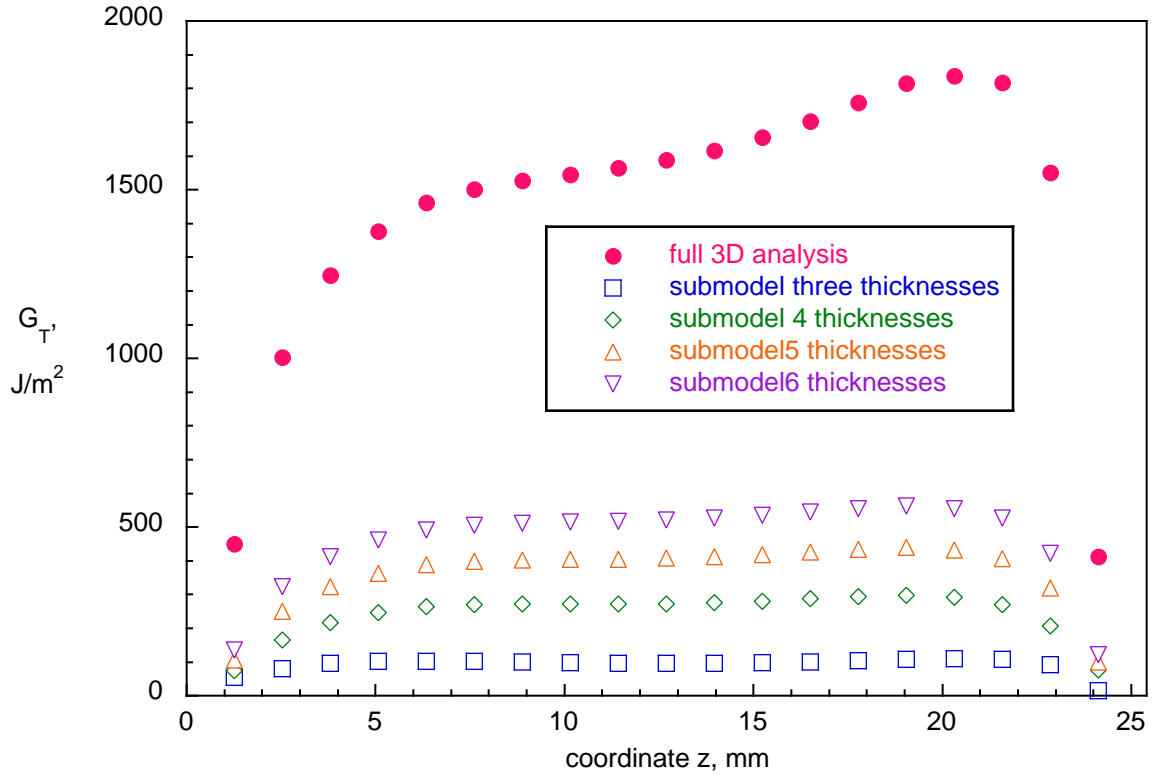


Figure 41. Computed total energy release rate across the width of the specimen at $x = 31.2$ mm for three-point bending test.

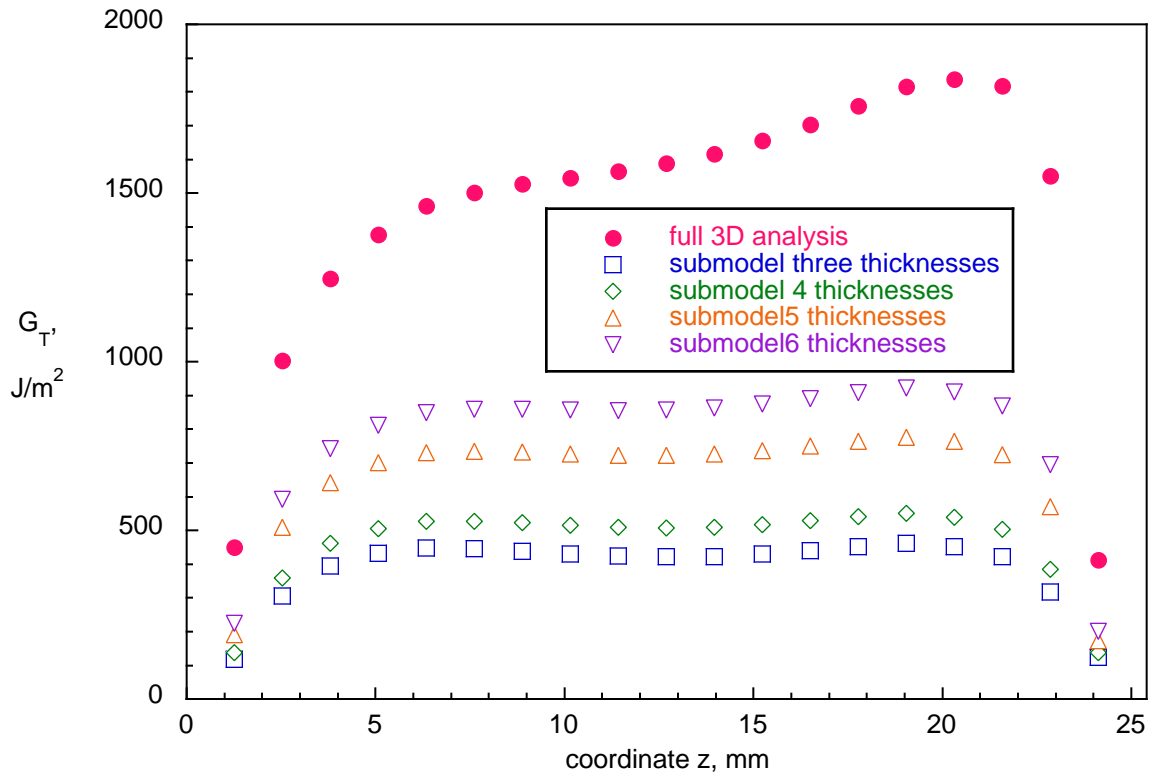


Figure 42. Computed total energy release rate across the width of the specimen at $x = 31.2$ mm for three-point bending test.

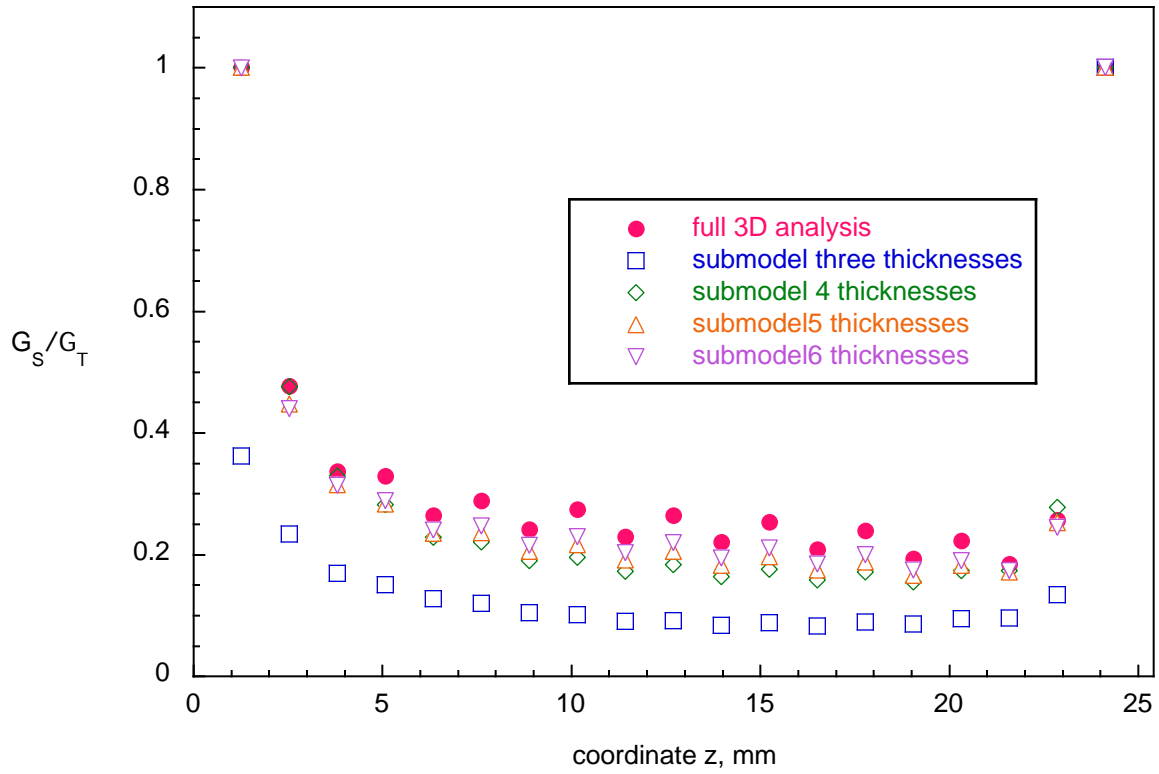


Figure 43. Computed mixed mode ratio across the width of the specimen at $x = 31.2$ mm for three-point bending test.

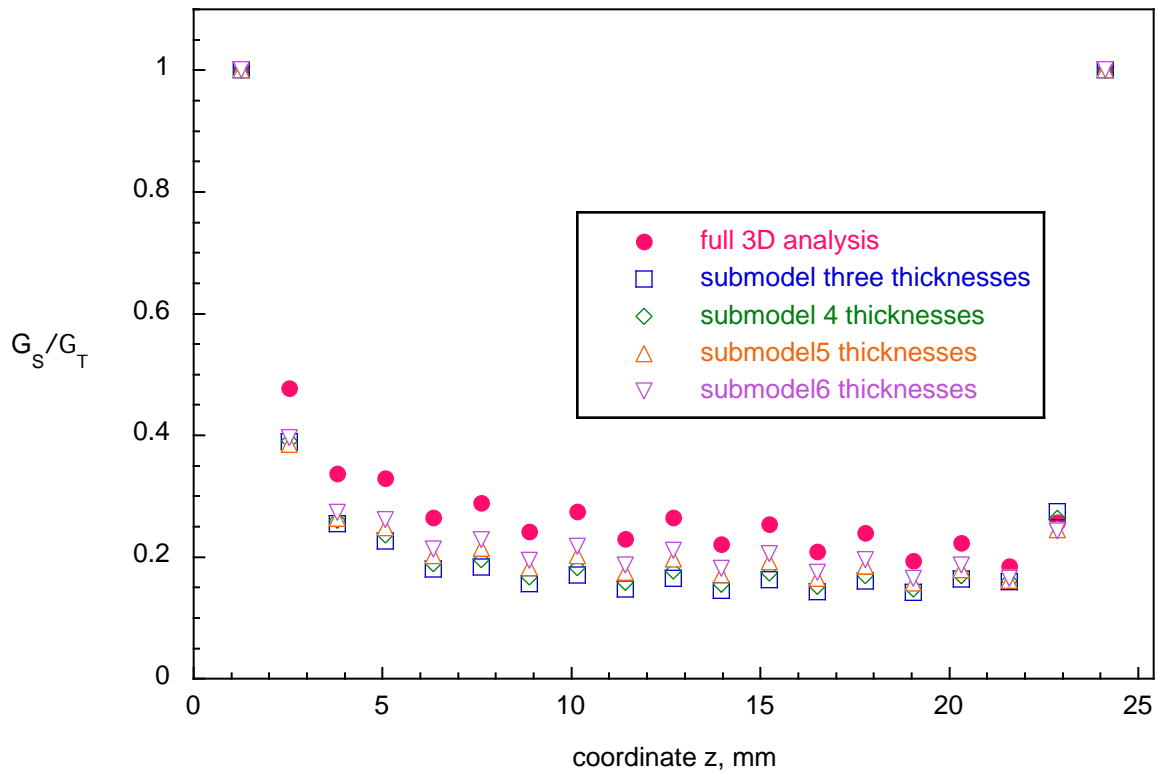


Figure 44. Computed mixed mode ratio across the width of the specimen at $x = 31.2$ mm for three-point bending test.

REPORT DOCUMENTATION PAGE				<i>Form Approved</i> <i>OMB No. 0704-0188</i>	
<p>The public reporting burden for this collection of information is estimated to average 1 hour per response, including the time for reviewing instructions, searching existing data sources, gathering and maintaining the data needed, and completing and reviewing the collection of information. Send comments regarding this burden estimate or any other aspect of this collection of information, including suggestions for reducing this burden, to Department of Defense, Washington Headquarters Services, Directorate for Information Operations and Reports (0704-0188), 1215 Jefferson Davis Highway, Suite 1204, Arlington, VA 22202-4302. Respondents should be aware that notwithstanding any other provision of law, no person shall be subject to any penalty for failing to comply with a collection of information if it does not display a currently valid OMB control number.</p> <p>PLEASE DO NOT RETURN YOUR FORM TO THE ABOVE ADDRESS.</p>					
1. REPORT DATE (DD-MM-YYYY)		2. REPORT TYPE		3. DATES COVERED (From - To)	
4. TITLE AND SUBTITLE				5a. CONTRACT NUMBER	
				5b. GRANT NUMBER	
				5c. PROGRAM ELEMENT NUMBER	
6. AUTHOR(S)				5d. PROJECT NUMBER	
				5e. TASK NUMBER	
				5f. WORK UNIT NUMBER	
7. PERFORMING ORGANIZATION NAME(S) AND ADDRESS(ES)				8. PERFORMING ORGANIZATION REPORT NUMBER	
9. SPONSORING/MONITORING AGENCY NAME(S) AND ADDRESS(ES)				10. SPONSORING/MONITOR'S ACRONYM(S)	
				11. SPONSORING/MONITORING REPORT NUMBER	
12. DISTRIBUTION/AVAILABILITY STATEMENT					
13. SUPPLEMENTARY NOTES					
14. ABSTRACT					
15. SUBJECT TERMS					
16. SECURITY CLASSIFICATION OF:			17. LIMITATION OF ABSTRACT	18. NUMBER OF PAGES	19b. NAME OF RESPONSIBLE PERSON
a. REPORT	b. ABSTRACT	c. THIS PAGE			19b. TELEPHONE NUMBER (Include area code)